MTLA 40 (2025) 102384

Contents lists available at ScienceDirect

Materialia

journal homepage: www.elsevier.com/locate/mtla

Full length article

Benchmarking advanced multiphase field modeling of Inconel 625 in additive manufacturing: Correlating powder bed fusion with dendrite growth and crack formation

Roya Darabi [a,b,*], João Pedro Oliveira [c], Narguess Nemati [d], Ana Reis [a], Jose Cesar de Sá [a]

[a] Faculty of Engineering, University of Porto (FEUP), Rua Dr. Roberto Frias, 400, Porto, 4200-465, Portugal
[b] Associate Laboratory for Energy, Transports and Aerospace (LAETA), Faculty of Engineering, University of Porto (FEUP), Porto, Portugal
[c] CENIMAT-i3N - Department of Materials Science, School of Science and Technology, NOVA University Lisbon, Caparica, Lisbon, 2825-097, Portugal
[d] Department of Mechanical and Production Engineering, Aarhus University, Katrinebjergvej, 8200 Aarhus N, Building 5126, Room 244, Aarhus, 8200, Denmark

ARTICLE INFO

Keywords:
Powder bed fusion
Finite element method (FEM)
Multiscale modeling
Phase-field
Multiphysics object-oriented simulation environment (MOOSE)
Dendrite growth
Liquation cracks
Inconel 625

ABSTRACT

This study provides a comprehensive thermomechanical simulation framework and mapping for the Powder Bed Fusion (PBF) process, with a primary focus on melt pool characterization. It also correlates the cooling behavior to the dendrite growth and some induced imperfections, such as crack evolution that stem from segregation at the grain boundaries. Utilizing the Allen-Cahn phase field formulation combined with an elastoplastic material model based on J2 plasticity, simulations are conducted within the finite element structure of the Multi-physics Object-Oriented Simulation Environment (MOOSE). An adaptive mesh refinement (AMR) strategy ensures precise modeling of the solidification front and powder melting during the interaction between the laser heat source and the powder. Key insights are gained from simulations of Inconel 625 thin plates and benchmarks, exploring the effects of temperature and phase changes on melt pool dimensions. A multi-application framework is developed to automatically transfer the temperature and cooling rate behavior of a representative part to the solidification application. The research addresses critical challenges in PBF, such as liquation cracking, and introduces a novel approach for information transfer between parent and child models, particularly for dendrite growth in a surrogate Ni–Nb–Al ternary system. This transfer incorporates solidification data, including temperature gradients and cooling velocities, enabling detailed predictions of low melting phase-induced liquation cracks. Experimental validation through single-track laser melting on Inconel 625 demonstrates reasonable alignment between melt pool dimensions obtained from simulations and experiments under various laser power and scan speed conditions. Additional phase-field simulations predict microstructural segregation and cellular features along melt pool boundaries under changing solidification dynamics, further enriched by the first phase-field model at the melt pool scale. By integrating computational modeling, experimental validation, and multiscale analysis, this work advances the understanding of PBF processes and additive manufacturing, offering insights into melt pool behavior, defect mitigation, and microstructure development.

1. Introduction

1.1. Motivation and significance

The motivation and significance of this paper lie in the urgent need to gain a comprehensive understanding of process parameters in additive manufacturing (AM), addressing both macro and microscale phenomena, especially within ternary Ni-Nb-Al alloys. These alloys hold immense potential for a range of high-performance applications, yet their behavior during AM processes remains largely poorly understood. Through the employment of phase-field modeling at both macro and micro levels, coupled with access to chemical information via the CALPHAD library, our study aims to unravel the complexities of melt pool formation and dendrite growth during AM processes. This endeavor is critical as these phenomena directly dictate the final properties and quality of manufactured components. By integrating CALPHAD-based modeling with chemical insights, we aspire to bridge the gap between experimental observations and theoretical predictions, fostering a deeper understanding of the chemical interactions within these alloys. Furthermore, by elucidating the intricate relationship

---

* Corresponding author.
E-mail address: rdarabi@fe.up.pt (R. Darabi).

https://doi.org/10.1016/j.mtla.2025.102384
Received 21 November 2024; Accepted 2 March 2025

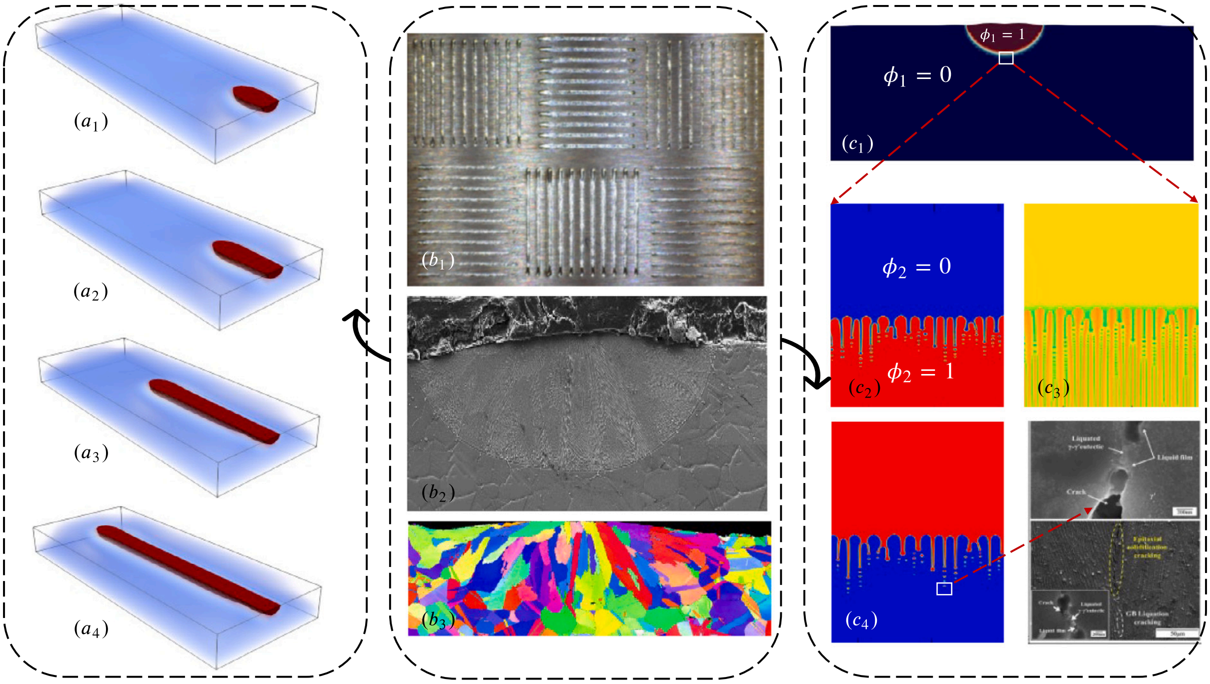

Fig. 1. Schematic depiction of solidification phenomena in the multiphysics process during laser powder bed fusion (PBF): $(a_1 - a_4)$: Evolution of the melt pool as the laser passes, $(b_1 - b_3)$: NIST benchmarks [1], including printed single lines and cross-sectional views, along with an Electron Backscatter Diffraction (EBSD) map of grains, $(c_1 - c_4)$: Critical points in solidification at the tail of the melt pool, highlighting parameters involved in solidification and the concentration of Al in the Ni matrix, as well as the contribution of elastic energy to the initiation of cracks. The phase evolution of γ-γ' is illustrated based on experimental observations in SEM micrographs of liquid films near liquation cracks in an as-deposited DED Inconel 738 sample from [2].

between process parameters and defect formation, notably cracks, our research endeavors to offer invaluable insights for defect mitigation and the enhancement of reliability and performance in AM-produced parts. To tackle these challenges, we propose a multiphysics modeling framework that integrates a finite element thermal model with an efficient phase-field method. The first model involves a phase-field approach to predict phase changes in the material during deposition, coupled with a mechanical model to incorporate the necessary interactions. Then, the thermal information, including the cooling rate of a representative domain, is automatically transferred to another level of the phase-field model to simulate the solidification of a ternary Ni-Nb-Al alloy system. At this level, the Allen-Cahn formulation governs the transition between liquid and solid phases, while the Cahn-Hilliard equation controls the elemental concentration, using thermodynamic data from the CALPHAD library. Then, the thermal information, including the cooling rate of a representative domain, is automatically transferred to another level of the phase-field model to simulate the solidification of a ternary Ni-Nb-Al alloy system. This framework aims to predict solidification microstructures and non-equilibrium chemical partitioning during laser powder bed fusion (LPBF) processing of Ni-Nb-Al-based alloys. Our micro phase field model, leverages thermodynamic factors to significantly enhance computational efficiency, rather than relying on Newton–Raphson methods, as seen in models that directly employ free energies from CALPHAD databases.. Using a ternary Ni-Nb-Al alloy as a case study, our investigation delves into site-specific grain evolution, with a primary focus on primary dendrite arm spacing (PDAS) and microsegregation. Additionally, we aim to explore the influence of laser power and scanning velocity across the melt pool, as well as the solidification parameters on the precipitation between dendrites and liquid pockets. This precipitation initiates the formation of porosity and induces cracks, which are critical factors in determining the overall quality and integrity of AM-produced components. The schematic view of research is shown in Fig. 1.

1.2. *Crack formation in Nickel-based superalloys*

Nickel-based superalloys are prone to various crack defects during high-energy beam additive manufacturing (HEB-AM), including solidification cracks, liquation cracks, strain-age cracks, ductility-dip cracks, and cold cracks [3,4] (Fig. 2). Solidification and liquation cracks are linked to liquid presence, while others occur in the solid state. Distinguishing between these cracks can be challenging due to overlapping characteristics [5].

Solidification Cracks: These cracks, or “hot tears” form in the mushy zone during solidification, often along high-angle grain boundaries due to stress concentration in interdendritic regions [6,7]. Rapid cooling and alloy composition significantly influence their formation [8,9] (Fig. 2). **Liquation Cracks:** Liquation cracks occur in the partially melted zone adjacent to the weld metal fusion zone. These cracks often form due to the remelting of low-melting-point phases under residual stress [10,11], as shown in Fig. 3. They are associated with microsegregation and rapid solidification, making liquid feeding difficult [12,13]. Rapid heating during the high energy heat source AM process contributes to the dissolution of certain grain-boundary phases, such as the γ-γ' eutectic and low-melting-point carbides, as shown in Fig. 4. Under significant residual stresses, these liquid films tend to act as initiation sites for cracks in the fabricated material. [10,11,14]. (Fig. 4).

Relationship Between Cracks: Solidification and liquation cracks are interconnected, with stress concentrations at grain boundaries often exacerbating crack formation [15]. Other crack types, such as strain-age and ductility-dip cracks, occur in the solid state and are influenced by residual stresses and material ductility [3,4].

1.3. *Phase-field modeling in additive manufacturing*

Phase-field (PF) modeling has emerged as a powerful tool for simulating microstructure evolution in additive manufacturing (AM) processes due to its thermodynamic consistency and ability to predict complex grain morphologies without explicit interface tracking [16,17].

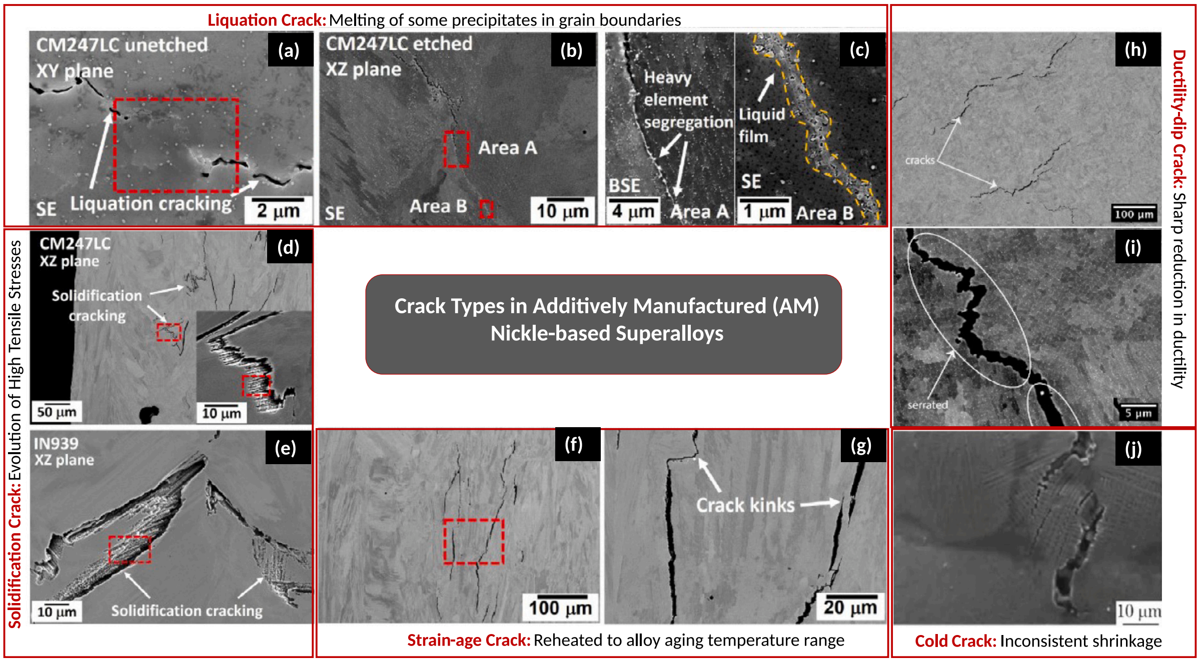

Fig. 2. Primary crack categories in nickel-based superalloys fabricated using AM: (a–c) Liquation cracks, (d–e) Solidification cracks, (f–g) Strain-age cracks, (h–i) Ductility-dip cracks, and (j) Cold cracks [3–5].

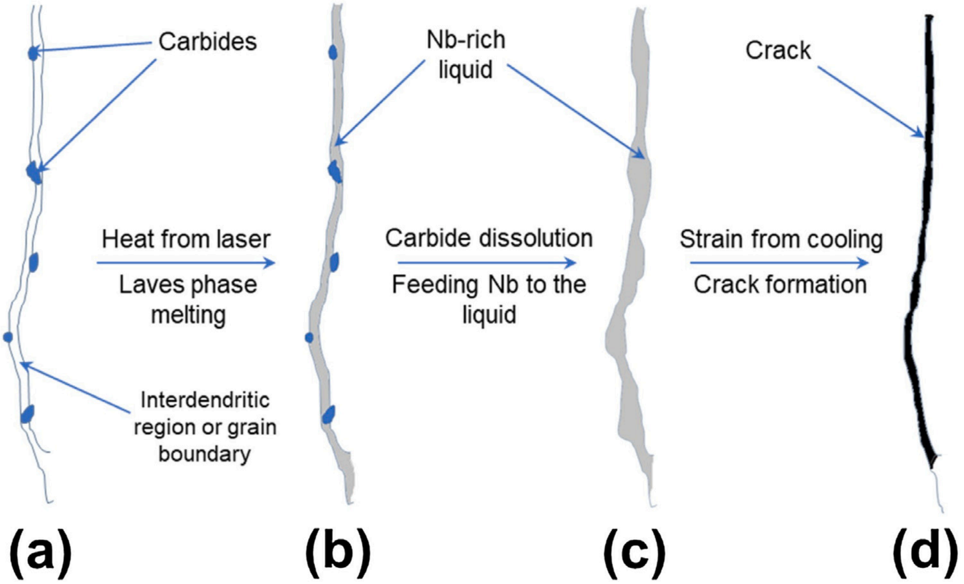

Fig. 3. Schematic diagrams illustrating crack formation due to the remelting of the Laves phase and the dissolution of NbC [12,13,15].

Recent advancements integrate PF models with CALPHAD for enhanced accuracy, though computational efficiency remains a challenge [18]. A multiphysics framework combining finite element thermal models with PF methods has been proposed to predict solidification microstructures and chemical partitioning in Ni-Nb-Al alloys during powder bed fusion (PBF) [19]. This approach focuses on predicting melt pool evolution by incorporating a high-density laser heat source into a thermo-elastoplastic-phase field model [20]. This model accounts for phase changes in the material across various phases, enabling accurate melt pool estimation through adaptive mesh refinement. Additionally, a micro-phase field model coupled with the CALPHAD library is developed to predict primary dendrite arm spacing (PDAS) and microsegregation, leveraging simplified free energy density for computational efficiency [20]. Furthermore, micro-scale PF modeling within the MOOSE framework explores the effects of process parameters on microstructure evolution, particularly in liquid pockets and dendrite-induced cracking [21,22]. These insights aim to optimize AM processes for high-performance Ni-Nb-Al-based alloys, ensuring superior mechanical properties and microstructural integrity [23,24].

2. Mathematical description

2.1. Macro phase field process modeling in AM application

In this work, a fully coupled, thermodynamically-consistent phase-field thermo-mechanical modeling approach for PBF is presented [25–27]. Consider a solid domain $\Omega \in \mathbb{R}^3$. At each material point $x \in \Omega$

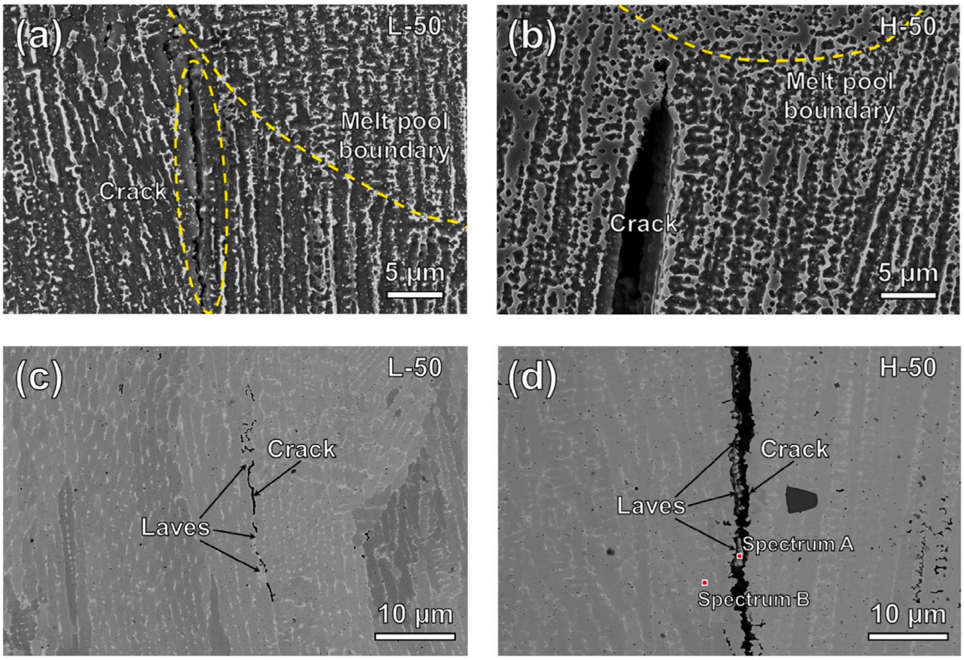

Fig. 4. Liquation cracking characteristics in Inconel 718, including SEM images, (a) and (b): high-magnification SEM images highlighting cracks in the microstructure, (c) and (d): showing cracks about Laves phase formations due to intermetallic compounds. [12,13,15].

and time $t \in [0, \tau]$, the thermomechanical problem is described by the following field variables:

$$u : \begin{cases} \Omega \times \tau \mapsto \mathbb{R}^d \\ (\mathbf{x}, t) \mapsto u(\mathbf{x}, t) \end{cases} \quad T : \begin{cases} \Omega \times \tau \mapsto R \\ (\mathbf{x}, t) \mapsto T(\mathbf{x}, t) \end{cases} \quad \phi : \begin{cases} \Omega \times \tau \mapsto [0,1] \\ (\mathbf{x}, t) \mapsto \phi(\mathbf{x}, t) \end{cases} \tag{1}$$

Where u, T, and ϕ respectively represent the displacement vector, temperature, and phase-field variables. The phase changing setting in the present work considers $\phi = 0$ and $\phi = 1$ as the soft (liquid) powder and hard (solid) powder states, respectively, while $0 < \phi < 1$ represents the in-between mushy phase zone. Following the infinitesimal deformation theory, whereby $\varepsilon = \nabla_s u = \frac{1}{2}(\nabla u + (\nabla u)^T)$, the total strain tensor ε can be additively decomposed into elastic (ε^e), plastic (ε^p), and thermal (ε^{th}) strain tensors, such that $\varepsilon = \varepsilon^e + \varepsilon^p + \varepsilon^{th}$. The thermoelastoplastic problem is described by the following set of independent state variables $V_1 = \{\varepsilon, \varepsilon^p, \alpha, T, \nabla T, \phi_1, \nabla\phi_1\}$, where α, T, ∇T, ϕ_1, $\nabla\phi_1$ are equivalent plastic strain, temperature, temperature gradient, phase field, and phase field gradient, respectively [25–30]. The free energy density function per unit volume can be written as;

$$\psi(V_1) = \psi^e + \psi^p + \psi^{th-e} + \psi^{th} + \psi^{\phi_1} \tag{2}$$

where ψ^e, ψ^p, ψ^{th-e}, ψ^{th}, and ψ^{ϕ_1} are the elastic, plastic, thermoelastic, pure thermal, and phase-field energy contributions [31]. The free energy terms can be detailed as:

$$\begin{cases} \text{(a)} \quad \psi^e = \dfrac{K}{2}\varepsilon_v^2 + \mu\varepsilon_d^e : \varepsilon_d^e \\ \text{(b)} \quad \psi^p = \sigma_y \alpha + \dfrac{1}{2} H \alpha^2 \\ \text{(c)} \quad \psi^{th-e} = -3K\xi\varepsilon_v(T - T_0) \\ \text{(d)} \quad \psi^{th} = c[(T - T_0) - T\ln(T/T_0)] \\ \text{(e)} \quad \psi^{\phi_1} = f(\phi_1, T) + \dfrac{\varepsilon_{\phi_1}^2}{2}\|\nabla\phi_1\|^2 \end{cases} \tag{3}$$

where K, μ are, respectively, the bulk and shear moduli, $\varepsilon_v = \mathrm{tr}(\varepsilon^e)$ is the volumetric strain and $\varepsilon_d^e = (\varepsilon^e - \frac{1}{3}\varepsilon_v I)$ is the deviatoric elastic strain tensor. Within the plastic energy term, σ_y and H are the initial yield stress and hardening modulus respectively. The remainder of the parameters are ξ as the thermal expansion coefficient, T_0 as the reference temperature, c as the heat capacity per unit volume and I as a second-order identity tensor. In the expression of the phase field energy, ψ^{ϕ_1}, the bulk free energy contribution $f(\phi_1, T)$ is added to the interfacial energy density as the local dissipation term, consisting of the phase-field gradient term and its coefficient ε_{ϕ_1}, which will be further explored in the next section. The time rate of the free energy can be obtained as follows:

$$\dot{\psi} = \frac{\partial\psi}{\partial\varepsilon^e} : \dot{\varepsilon} - \frac{\partial\psi}{\partial\varepsilon^p} : \dot{\varepsilon}^p + \frac{\partial\psi}{\partial\alpha}\dot{\alpha} + \frac{\partial\psi}{\partial T}\dot{T} + \frac{\partial\psi}{\partial\nabla T}.\nabla\dot{T} + \frac{\partial\psi}{\partial\phi_1}\dot{\phi}_1 + \frac{\partial\psi}{\partial\nabla\phi_1}.\nabla\dot{\phi}_1 \tag{4}$$

By using the divergence theorem, the last term in the above equation can be written as:

$$\frac{\partial\psi}{\partial\nabla\phi_1}.\nabla\dot{\phi}_1 = \mathrm{div}(\dot{\phi}_1 \frac{\partial\psi}{\partial\nabla\phi_1}) - \mathrm{div}(\frac{\partial\psi}{\partial\nabla\phi_1})\dot{\phi}_1 \tag{5}$$

To obtain thermodynamically consistent constitutive relations governing the coupled thermomechanical problem, the second law of thermodynamics (entropy inequality) is used which can be interpreted in the form of the following generalized Clausius–Duhem inequality [32] per unit volume as:

$$\sigma : \dot{\varepsilon} - \dot{\psi} - s\dot{T} - \frac{1}{T}q.\nabla T \geq 0 \tag{6}$$

In the context of continuum mechanics, the stress tensor σ, entropy density s, and heat flux vector q play pivotal roles. Ensuring thermodynamic equilibrium is paramount and is captured by various equations and inequalities. Substituting Eqs. (4) and (5) into the inequality in Eq. (6), we obtain:

$$(\sigma - \frac{\partial\psi}{\partial\varepsilon^e}) : \dot{\varepsilon} + \frac{\partial\psi}{\partial\varepsilon^p}\dot{\varepsilon}^p - \frac{\partial\psi}{\partial\alpha}\dot{\alpha} - (s + \frac{\partial\psi}{\partial T})\dot{T} - \frac{\partial\psi}{\partial\nabla T}.\nabla\dot{T}$$
$$-\left(\frac{\partial\psi}{\partial\phi_1} - \mathrm{div}\frac{\partial\psi}{\partial\nabla\phi_1}\right)\dot{\phi}_1 - \frac{1}{T}q \cdot \nabla T \geq 0. \tag{7}$$

This inequality must hold for any arbitrary thermodynamic process. With insights from Colman's thermodynamic framework [25,26], equilibrium equations can be derived:

$$\sigma = \frac{\partial\psi}{\partial\varepsilon^e} = K(e - \xi(T - T_0))I + 2\mu\varepsilon_d^e, \tag{8}$$

$$s = -\frac{\partial\psi}{\partial T} = 3K\xi e + c\ln\left(\frac{T}{T_0}\right) + \rho L\left(\frac{1}{T_M}\right)p(\phi_1), \tag{9}$$

$$\frac{\partial \psi}{\partial \nabla T} = 0, \tag{10}$$

$$\int_{\Omega} \operatorname{div}\left(\dot{\phi}_1 \frac{\partial \psi}{\partial \nabla \phi_1}\right) d\Omega = \int_{\partial\Omega} \dot{\phi}_1 \frac{\partial \psi}{\partial \nabla \phi_1} \cdot \mathbf{n}\, d\partial\Omega, \tag{11}$$

$$\dot{\phi}_1 \frac{\partial \psi}{\partial \nabla \phi_1} \cdot \mathbf{n} = 0. \tag{12}$$

Further, the dissipative inequalities stemming from Eq. (7) are delineated:

$$-\frac{1}{T} q \cdot \nabla T \geq 0, \tag{13}$$

$$-\left(\frac{\partial \psi}{\partial \phi_1} - \operatorname{div} \frac{\partial \psi}{\partial \nabla \phi_1}\right) \dot{\phi}_1 \geq 0, \tag{14}$$

$$\frac{\partial \psi}{\partial \varepsilon^p} : \dot{\varepsilon}^p - \frac{\partial \psi}{\partial \alpha} \dot{\alpha} \geq 0. \tag{15}$$

Eq. (13) describes thermal dissipation using Fourier's law, while Eq. (15) encapsulates mechanical dissipation via the Clausius–Planck inequality [33]. Utilizing thermodynamically consistent approaches akin to Ginzburg–Landau theory, the variation of phase-field energy density, as denoted by Eq. (3e), yields equilibrium equations:

$$\frac{\delta \psi^{\phi_1}}{\delta \phi_1} = \frac{\partial f}{\partial \phi_1} - \varepsilon_{\phi_1}^2 \nabla^2 \phi_1 = 0. \tag{16}$$

The evolution of the phase-field parameter ϕ_1 is aptly described by the time derivative of a non-conserved variable η, akin to the Allen-Cahn equation [34,35]:

$$\frac{\partial \eta}{\partial t} = -M \frac{\partial F}{\partial \eta}. \tag{17}$$

Here, F represents the free energy functional encompassing local and gradient terms for conserved and non-conserved field variables. The evolution of ϕ_1 is described by:

$$\frac{\partial \phi_1}{\partial t} = -M \left[\frac{\partial f}{\partial \phi_1} - \frac{l^2}{2} \nabla^2 \phi_1\right]. \tag{18}$$

The interface mobility parameter M is defined as [34]:

$$M = \frac{\mu_{\phi_1} T_M}{6 \delta \rho L}, \tag{19}$$

with μ_{ϕ_1} and δ representing the interface kinetic coefficient and interface width, respectively. The choice of $f(\phi_1, T)$ determines the free energy density, encapsulating the energy barrier at the interface and the difference of free energy terms between phases. The finite element (FE) simulation requires choosing an element size smaller than δ to ensure resolution at the solid–liquid interface [34]. Eq. (16) introduces the phase-field gradient coefficient ε_{ϕ_1}, representing the diffusive interface width l. Drawing from previous research [31], we define the system's free energy density as:

$$f(\phi_1, T) = W g(\phi_1) + \Theta(T) p(\phi_1), \tag{20}$$

where W is the interfacial energy barrier determined by the surface tension ω and δ. Additionally, $\Theta(T)$ accounts for the thermal driving force for phase changes. This formulation captures the competition between energy barriers at the solid–liquid interface and associated free energy differences. The free energy associated with the phase-field variable, ψ^{ϕ_1}, is redefined from Eq. (21), incorporating the defined functions:

$$\psi^{\phi_1} = W g(\phi_1) + \rho L \left(\frac{T_M - T}{T_M}\right) p(\phi_1) + \frac{l^2}{2} \|\nabla \phi_1\|^2. \tag{21}$$

Here, $g(\phi_1)$ and $p(\phi_1)$ represent the double well potential and interpolating function, respectively, chosen from [34]. The evolution of the phase-field variable, as expressed in Eq. (18), is given by:

$$\frac{\partial \phi_1}{\partial t} = -M \left[W g'(\phi_1) + \rho L \left(\frac{T_M - T}{T_M}\right) p'(\phi_1) - \operatorname{div}(l^2 \nabla \phi_1)\right]. \tag{22}$$

In the absence of external forces, the balance of linear momentum yields:

$$\nabla \sigma = 0. \tag{23}$$

The elastic strain tensor's dual, σ, is defined as:

$$\sigma = \frac{\partial \psi}{\partial \varepsilon^e} = C^e \varepsilon^e, \tag{24}$$

where C^e denotes the fourth-order elastic stiffness tensor. The elastic stress σ can be expressed alternatively in terms of strains and thermal strains, as represented by Eq. (24). The energy balance equation and entropy evolution stem from the first law of thermodynamics, conserving internal energy:

$$\dot{E} = \sigma : \dot{\varepsilon} - \nabla \cdot q + Q, \tag{25}$$

where E is the specific internal energy and Q is the external heat supply [20]. Using the Legendre transform, the internal energy converts to the sum of free energy and entropy-temperature potentials, The specific internal energy E is expressed as $E = \psi + sT$, and its rate form is given by:

$$\dot{E} = \dot{\psi} + s\dot{T} + \dot{s}T. \tag{26}$$

Referring to the inequality in Eq. (12), the rate of the free energy, as described in Eq. (4), is redefined as:

$$\dot{\psi} = \sigma : \dot{\varepsilon} - D - s\dot{T} + \left[\frac{\partial \psi}{\partial \phi_1} - \operatorname{div}\left(\frac{\partial \psi}{\partial \nabla \phi_1}\right)\right] \dot{\phi}_1. \tag{27}$$

Utilizing Eqs. (21) and (27), along with the internal energy rate forms in Eqs. (26) and (27), we obtain:

$$T\dot{s} = D - \left[W g'(\phi_1) + \rho L \left(\frac{T_M - T}{T_M}\right) p'(\phi_1) - \operatorname{div}(l^2 \nabla \phi_1)\right] \dot{\phi}_1 - \operatorname{div} q + Q, \tag{28}$$

where $s = -\frac{\partial \psi}{\partial T}$. Similarly, deriving the time rate of the entropy density s, using the chain rule and rearrangements, leads to:

$$\begin{aligned} \dot{s} = &-\frac{\partial(\sigma : \dot{\varepsilon} - D)}{\partial T} - \frac{\partial^2 \psi}{\partial T^2} \dot{T} \\ &- \frac{\partial}{\partial T} \left[W g'(\phi_1) + \rho L \left(\frac{T_M - T}{T_M}\right) p'(\phi_1) - \operatorname{div}(l^2 \nabla \phi_1)\right] \dot{\phi}_1. \end{aligned} \tag{29}$$

Substituting Eq. (29) into Eq. (28) results in:

$$c\dot{T} = D + W^{ep} - W^{\phi_1} - \operatorname{div} q + Q, \tag{30}$$

where,

$$c = -T \frac{\partial^2 \psi}{\partial T^2}, \tag{31}$$

$$W^{ep} = T \frac{\partial(\sigma : \dot{\varepsilon} - D)}{\partial T}, \tag{32}$$

and

$$\begin{aligned} W^{\phi_1} = &\left[\rho L \left(\frac{T}{T_M}\right) p'(\phi_1) + W g'(\phi_1)\right. \\ &\left. + \rho L \left(\frac{T_M - T}{T_M}\right) p'(\phi_1) - \operatorname{div}(l^2 \nabla \phi_1)\right] \dot{\phi}_1. \end{aligned} \tag{33}$$

Here, c represents the volumetric heat capacity, and W^{ep}, W^{ϕ_1} and D denote the contributions related to elastoplastic and phase-field problems, the plastic dissipative term [27], respectively. In what follows, a brief overview of associative rate-independent J_2 plasticity theory using an isotropic hardening law is given, which is employed herein to allow for plastic deformations within the constitutive model [36]. The standard yield function using the von Mises criterion is given by:

$$f_y(\sigma_d, q^\alpha, T) := \sigma_{\mathrm{eq}} - Y(\alpha), \tag{34}$$

where $Y(\alpha) = \sigma_Y - q^\alpha$ with σ_Y as the material yield stress and $\sigma_{\mathrm{eq}} = \sqrt{3J_2} = \left(\frac{3}{2}\sigma_d : \sigma_d\right)^{\frac{1}{2}}$ is the equivalent von Mises stress, in which $\sigma_d = \sigma - \frac{1}{3}\mathrm{tr}(\sigma) I$ is the deviatoric stress tensor. The rate of the stress tensor can be given, according to Eq. (8), as:

$$\dot{\sigma} = C^e (\dot{\varepsilon} - \dot{\varepsilon}^p + \dot{\varepsilon}^{th}), \tag{35}$$

where C^e is the elasticity tensor. The rate of the plastic strain can be defined via the associative flow rule:

$$\dot{\varepsilon}^p = \dot{\lambda}\left(\frac{\partial f_y}{\partial \sigma}\right), \tag{36}$$

where $\dot{\lambda}$ is the plastic multiplier and $\left(\frac{\partial f_y}{\partial \sigma}\right)$ indicates the direction of the plastic strain increment. Using the chain rule, the time derivative of the yield function reads:

$$\dot{f}_y = \left(\frac{\partial f_y}{\partial \sigma} : \dot{\sigma}\right) + \left(\frac{\partial f_y}{\partial \bar{q}} : \dot{\bar{q}}\right), \tag{37}$$

Following this, the accumulated (equivalent) plastic strain can be written as:

$$\bar{\varepsilon}^p = \left(\frac{2}{3}\varepsilon^p : \varepsilon^p\right)^{\frac{1}{2}}, \tag{38}$$

The plastic consistency parameter must satisfy the Kuhn–Tucker conditions given by:

$$\begin{aligned} &\dot{\lambda} \geq 0, \\ &\dot{\lambda} f_y = 0, \\ &f_y \leq 0. \end{aligned} \tag{39}$$

2.2. Micro phase field modeling in micro-structure simulation

In this section of this work, a thermodynamically-consistent phase-field chemical modeling approach for dendrite growing is presented [37]. Consider a solid domain $\Omega \in \mathbb{R}^3$. At each material point $x \in \Omega$ and time $t \in [0, \tau]$, the thermochemical problem is described by the following field variables:

$$\begin{cases} c : \Omega \times \tau \mapsto \mathbb{R} \\ (\mathbf{x}, t) \mapsto c(\mathbf{x}, t) \end{cases} \quad \text{and} \quad \begin{cases} \phi_2 : \Omega \times \tau \mapsto [0, 1] \\ (\mathbf{x}, t) \mapsto \phi_2(\mathbf{x}, t) \end{cases} \tag{40}$$

Where c and ϕ_2 respectively represent the concentration and phase-field variables. The phase-changing setting in the present work is similar to what was presented in Section 2.1 but on another computational scale. The thermo-chemical problem is described by the following set of independent state variables $V_2 = \{c, \phi_2, \nabla\phi_2\}$, where c, ϕ_2, $\nabla\phi_2$ are concentration, phase field, and phase field gradient, respectively. The free energy density function per unit volume can be written as;

$$\psi(V_2) = \psi^{Ch} + \psi^{Int} \tag{41}$$

where ψ^{Ch}, and ψ^{Int} are chemical, and Interfacial energy contributions [31]. The free energy terms can be detailed as:

$$\begin{cases} \text{(a)} \quad \psi^{Ch} = p(\phi_2) G^S(c_1^S, c_2^S, T) + (1 - p(\phi_2)) G^L(c_1^L, c_2^L, T) \\ \text{(b)} \quad \psi^{Int} = f(\phi_2, T) - \dfrac{a^2}{2}\|\nabla\phi_2\|^2 \end{cases} \tag{42}$$

In the first part of Eq. (42b), the double well potential term can be presented herein as:

$$f(\phi_2, T) = W g(\phi_2) \tag{43}$$

The second part of Eq. (42b), is the so-called gradient term. Next, we derive the time evolution equation of ϕ_2 by following the second law of thermodynamics. Because the phase field variable ϕ_2 is a non-conserved quantity, we use the Allen-Cahn equation [35].

$$\frac{\partial\phi_2}{\partial t} = -M_{\phi_2}\frac{\delta\psi(V_2)}{\delta\phi_2}, \tag{44}$$

where M_{ϕ_2} is the phase field mobility factor and the functional derivative $\frac{\delta\psi(V_2)}{\delta\phi_2}$ can be calculated as:

$$\frac{\delta\psi(V_2)}{\delta\phi_2} = \frac{\partial\psi^{Ch}}{\partial\phi_2} + \frac{\partial\psi^{dou}}{\partial\phi_2} - \nabla.\frac{\partial\psi^{grad}}{\partial\nabla\phi_2} \tag{45}$$

Based on previous researchers [38,39] in detail;

$$\frac{\delta\psi(V_2)}{\delta\phi_2} = p'(\phi)\left((G^S - G^L) + \frac{\partial G^S}{\partial c_1^S}(c_1^L - c_1^S) + \frac{\partial G^S}{\partial c_2^S}(c_2^L - c_2^S)\right) + W g'(\phi) \tag{46}$$

We obtain the time evolution equation of the phase-field variable ϕ_2 as follows;

$$\begin{aligned} \frac{\partial\phi_2}{\partial t} = \frac{W^2}{\tau_0 a(\theta)^2} \Big[&\nabla \cdot \left(a(\theta)^2 \nabla\phi_2\right) \\ &+ \frac{\partial}{\partial y}\left(|\nabla\phi_2|^2\right) a(\theta) \frac{\partial a(\theta)}{\partial(\partial_y\phi_2)} \\ &+ \frac{\partial}{\partial z}\left(|\nabla\phi_2|^2\right) a(\theta) \frac{\partial a(\theta)}{\partial(\partial_z\phi_2)} \\ &- \frac{1}{W^2}\frac{\partial g(\phi_2)}{\partial\phi_2} + \frac{a_1}{W\sigma}\frac{\partial p(\phi_2)}{\partial\phi_2}\Delta G_{ch}\Big] \end{aligned} \tag{47}$$

herein, W is the width of the interface, the function $g(\phi_2) = \phi_2^2(1 - \phi_2)^2$ represents a double-well potential ensuring the existence of two equilibrium states at $\phi_2 = 0$ and $\phi_2 = 1$, corresponding to the bulk phases. As for $p(\phi_2)$, it serves as an interpolation function. Here, we select $p(\phi_2) = \phi_2^3(10 - 15\phi_2 + 6\phi_2^2)$ due to its fulfillment of the necessary interpolation condition $p(0) = 1$, $p(1) = 1$, while also maintaining a vanishing slope at $\phi_2 = 0$ and $\phi_2 = 1$ to prevent any shift in the bulk states. The relaxation time τ_0 is linked to the physical quantities by [38]:

$$\tau_0 = a_1 a_2 W^3 \left(\chi_1^L \frac{\left|c_1^L - c_1^S\right|^2}{\sigma D_1^L} + \chi_2^L \frac{\left|c_2^L - c_2^S\right|^2}{\sigma D_2^L}\right) \tag{48}$$

where $a_1 = \sqrt{(2)}/3$ and $a_2 = 1.175$ [40] are the numerical constants and χ_A^L is the mean thermodynamic factor. The formulation for the four-fold surface energy anisotropy for FCC metals [41] is given by:

$$a(\theta) = 1 + \epsilon\cos^4(\theta + \theta_0) \tag{49}$$

where ϵ represents the anisotropy strength and in the y-z plane, we will have,

$$\theta = \arctan\left(\frac{\partial_z\phi_2}{\partial_y\phi_2}\right) \tag{50}$$

θ denotes the angle between the interface normal and the y-axis, and θ_0 indicates the misorientation angle between the preferred crystalline orientation and the temperature gradient direction. The driving force for solidification in this model is determined from the chemical free energy density, as described in [10,38].

$$\Delta G_{ch}(\phi_2, c) = \sum_A^N \chi_A^L(c_A^S - c_A^L)\frac{(c_A - c_A^{eq})}{\phi_2 + (1 - \phi_2)k_A^L} \tag{51}$$

The parameter χ_A^L represents the thermodynamic factor of the liquid phase and is defined as the second derivative of the free energy function from the database with respect to the solute equilibrium concentration. This formulation, based on the parabolic free energy model, circumvents the need for intensive computation of the driving force at each time-iteration using TQ-interface or extrapolation schemes [42]. Furthermore, its incorporation of derived thermodynamic factors eliminates the necessity for using unrealistic interpolated free energy functions [18]. Consequently, this phase-field method simultaneously ensures simulation accuracy and enhances modeling efficiency, particularly for multi-phase or multi-component systems. In this investigation, we assume that χ_A^L is constant within the freezing range for further simplification. The solute diffusion equation is expressed based on the Cahn-Hilliard equation [43]:

Table 1
Strong form equations governing the coupled problem.

Description
Momentum balance: $\nabla \cdot \sigma = 0$
Phase-field evolution: $\dot{\phi}_1 = -M\left[W g'(\phi_1) + \rho_L \left(\frac{T_M - T}{T_M}\right) p'(\phi_1) - \mathrm{div}(l^2 \nabla \phi_1)\right]$
Temperature evolution: $c\dot{T} = D + W^{\mathrm{ep}} - W^{\phi_1} - \mathrm{div} q + Q$

Table 2
Governing initial and boundary conditions.

Dirichlet B.C. (Γ_D)	$u(x,t) = u^*(x,t)$ on Γ_{D_u}
	$\phi_1(x,t) = \phi_1^*(x,t)$ on $\Gamma_{D_{\phi_1}}$ $T(x,t) = T^*(x,t)$ on Γ_{D_T}
Neumann B.C. (Γ_N)	$-\kappa \nabla T \cdot n = q$ on Γ_{N_T} $\nabla \phi_1 \cdot n = 0$ on $\Gamma_{N_{\phi_1}}$ $\sigma \cdot n = t^*$ on Γ_{N_u}
Initial conditions	$T = T_{\mathrm{ref}}$ on Γ_{N_T} $\phi_1 = \bar{\phi}_1$ on $\Gamma_{N_{\phi_1}}$ $u = \bar{u}$ on Γ_{N_u}

$$\frac{\partial c_A}{\partial t} = \nabla \cdot \left[\left(p(\phi_2) D_A^S \nabla c_A^S + (1 - p(\phi_2)) D_A^L \nabla c_A^L\right) + J_{at}\right] \tag{52}$$

J_{at} is the anti-trapping current used to eliminate spurious solute-trapping effects at the interface [44] and is expressed as:

$$J_{\mathrm{at}} = \sum_A^N \sqrt{\frac{W}{2}} (c_A^S - c_A^L) \frac{\nabla(\phi_2)}{\left|\nabla(\phi_2)\right|} \frac{\partial \phi_2}{\partial t} \tag{53}$$

The species concentration at any location for species A is given by:

$$c_A = p(\phi) c_A^S + (1 - p(\phi)) c_A^L \tag{54}$$

Eq. (53) assumes that the interpolation function $p(\phi)$ is also given by ϕ. Following the Kim-Kim-Suzuki (KKS) approach [45], it is assumed that the chemical potential for each species is the same in the solid and liquid phases, so that for each species A;

$$\frac{\partial G^S}{\partial c_A^S} = \frac{\partial G^L}{\partial c_A^L} \tag{55}$$

The concentrations c_A^S and c_A^Lin Eq. (55) are the solute concentrations at the diffuse interface. Eqs. (54) and (55) yield a set of 4 equations for a ternary alloy with two types of solutes.

2.3. Summary of the governing equations

2.3.1. Macro phase field process modeling in AM application

The coupled thermomechanical phase-field problem described in the previous section can be represented by the summary of the strong form equations given in Table 1 constrained by initial and boundary conditions (BCs) represented in Table 2, under the assumption of $\Gamma_D \cup \Gamma_N = \partial\Omega$ and $\Gamma_D \cap \Gamma_N = \emptyset$, with Γ_D and Γ_N indicating the Dirichlet- and Neumann-type boundaries, respectively.

2.3.2. Micro phase field modeling in micro-structure simulation

The thermomechanical micro phase-field problem discussed earlier, is encapsulated by the comprehensive set of equations detailed in Table 3, along with initial and boundary conditions (BCs) outlined in Table 4. These conditions specify Dirichlet and Neumann boundaries, respectively.

3. Numerical implementations

The finite element method (FEM) is utilized to implement the formulation outlined in the previous section by using the weak form of the governing PDEs given in provided Equations in Table 1.

$$\int_\Omega \sigma : \nabla \delta u \, d\Omega = 0 \tag{56}$$

$$\int_\Omega \left[\frac{1}{M}\dot{\phi}\delta\phi + W g'(\phi)\delta\phi + \rho_L \left(\frac{T_M - T}{T_M}\right) p'(\phi)\delta\phi + l^2 \nabla\phi \cdot \nabla\delta\phi\right] d\Omega - \int_{\Gamma_{N_\phi}} l^2 \nabla\phi \cdot n \delta\phi \, dS = 0 \tag{57}$$

$$\int_\Omega (c\dot{T} + W^\phi)\delta T \, d\Omega + \int_\Omega \kappa \nabla T \cdot \nabla \delta T \, d\Omega + \int_\Omega Q \delta T \, d\Omega = 0 \tag{58}$$

Using the standard FEM method, the field variables and their spatial derivatives are approximated at the element level as:

$$u = N_u \mathbf{u}_e, \qquad \epsilon = B_u \mathbf{u}_e, \tag{59}$$

$$\phi = N_{\phi_1} \boldsymbol{\phi}_{\mathbf{1}_e}, \qquad \nabla\phi_1 = B_{\phi_1} \boldsymbol{\phi}_{\mathbf{1}_e}, \tag{60}$$

$$T = N_T \mathbf{T}_e, \qquad \nabla T = B_T \mathbf{T}_e, \tag{61}$$

where $\mathbf{u}_e$, $\boldsymbol{\phi}_e$, and $\mathbf{T}_e$ are the nodal values of the displacements, phase-field, and temperature at an element e. For interpolation purposes, the standard shape function matrices N_u, N_ϕ, N_T and their corresponding

Table 3
Strong form equations governing the phase-field and concentration evolution.

Description
Phase-field evolution:
$\begin{aligned} \dot{\phi}_2 = \frac{W^2}{\tau_0 a(\theta)^2} \Bigg[& \nabla \cdot \left(a(\theta)^2 \nabla\phi_2\right) \\ & + \frac{\partial}{\partial y}\left(\lvert\nabla\phi_2\rvert^2 a(\theta) \frac{\partial a(\theta)}{\partial(\partial_y \phi_2)}\right) \\ & + \frac{\partial}{\partial z}\left(\lvert\nabla\phi_2\rvert^2 a(\theta) \frac{\partial a(\theta)}{\partial(\partial_z \phi_2)}\right) \\ & - \frac{1}{W^2} \frac{\partial g(\phi_2)}{\partial \phi_2} \\ & + \frac{a_1}{W\sigma} \frac{\partial p(\phi_2)}{\partial \phi_2} \sum_A^N \chi_A^L (c_A^S - c_A^L) \frac{(c_A - c_A^{eq})}{\phi_2 + (1 - \phi_2) k_A^L} \Bigg] \end{aligned}$
Concentration evolution:
$\begin{aligned} \dot{c_A} = \nabla \cdot \Bigg[& p(\phi_2) D_A^S \nabla c_A^S \\ & + (1 - p(\phi_2)) D_A^L \nabla c_A^L \\ & + \sum_A^N \sqrt{\frac{W}{2}} (c_A^S - c_A^L) \frac{\nabla(\phi_2)}{\left\lvert\nabla(\phi_2)\right\rvert} \frac{\partial\phi_2}{\partial t} \Bigg] \end{aligned}$

Table 4
Governing initial and boundary conditions.

Dirichlet B.C. (Γ_D)	$c_A(x,t) = c_A^*(x,t)$ on $\Gamma_{D_{c_A}}$ $\phi_2(x,t) = \phi_2^*(x,t)$ on $\Gamma_{D_{\phi_2}}$
Neumann B.C. (Γ_N)	$-\nabla c_A \cdot n = c_S - c_L$ on Γ_{N_c} $\nabla \phi_2 \cdot n = 0$ on $\Gamma_{N_{\phi_2}}$
Initial conditions	$c_A = c_{A_{\mathrm{ref}}}$ on $\Gamma_{N_{c_A}}$ $\phi_2 = \bar{\phi_2}$ on $\Gamma_{N_{\phi_2}}$

gradient operators B_u, B_ϕ, B_T are utilized. The residuals associated with the displacement field, phase field, and temperature field are given by:

$$r_u = \int_\Omega \sigma B_u^T \, dV - \int_{\Gamma_{N_u}} t^* N_u^T \, dS \tag{62}$$

$$\begin{aligned} r_\phi = \int_\Omega \Big[& \frac{1}{M} \dot{\phi} [N_\phi]^T N_\phi - 2W^\phi (1-\phi)(1-2\phi)[N_\phi]^T \\ & -30\Theta(T)\phi^2(1-\phi)^2 [N_\phi]^T + l^2 [B_\phi]^T [B_\phi] \Big] \, dV \\ & - \int_{\Gamma_{N_\phi}} l^2 [B_\phi]^T [B_\phi][N_\phi] \, dS \end{aligned} \tag{63}$$

$$\begin{aligned} r_T = \int_\Omega \Bigg(& c\dot{T} - \left[\rho_L \left(\frac{T}{T_M} \right) p'(\phi) + W g'(\phi) \right. \\ & + \left. \rho_L \left(\frac{T_M - T}{T_M} \right) p'(\phi) - \mathrm{div}(l^2 \nabla \phi) \right] \Bigg) [N_T] \, dV \\ & - \int_{\Gamma_{N_T}} \kappa [B_T]^T [N_T] \, dS + \int_\Omega \kappa [B_T]^T [B_T] \, dV + \int_\Omega Q [N_T]^T \, dV = 0 \end{aligned} \tag{64}$$

3.1. Micro phase field modeling in micro-structure simulation

In this process, arbitrary test functions linked with the field variables are utilized and multiplied by the corresponding PDEs, thereby yielding the weak forms as elaborated below.

$$\begin{aligned} & \int_\Omega \dot{\phi}_2 \delta\phi_2 \, dv - \frac{W^2}{\tau_0} \int_\Omega \Big[\nabla \delta\phi_2 \cdot \nabla \phi_2 \\ & + \delta\phi_2 \left(-\frac{1}{W^2} \frac{\partial g(\phi_2)}{\partial \phi_2} + \frac{a_1}{W\sigma} \frac{\partial p(\phi_2)}{\partial \phi_2} \Delta G_{ch} \right) \Big] \, dv = 0 \end{aligned} \tag{65}$$

$$\begin{aligned} & \int_\Omega \dot{c}_A \, \delta c_A \, dv + \int_\Omega \left[p(\phi_2) D_A^S \nabla c_A^S + (1 - p(\phi_2)) D_A^L \nabla c_A^L \right] \cdot \nabla \delta c_A \, dv \\ & - \sum_{A=1}^N \int_\Omega \nabla \cdot \left[\sqrt{\frac{W}{2}} (c_A^S - c_A^L) \frac{\nabla \phi_2}{|\nabla \phi_2|} \frac{\partial \phi_2}{\partial t} \right] \delta c_A \, dv = 0. \end{aligned} \tag{66}$$

To solve the coupled system of equations using the finite element method (FEM), follow these steps: - Discretize the domain Ω into finite elements. Define the mesh with nodes and elements. - Define the basis functions $\{\phi_i\}_{i=1}^N$ for the phase field and concentration fields. Approximate the solutions ϕ_2 and c_A using the basis functions:

$$c_A = N_{c_A} \mathbf{c}_{\mathbf{A}_e}, \qquad \nabla c_A = B_{c_A} \mathbf{c}_{\mathbf{A}_e}, \tag{67}$$

$$\phi = N_\phi \boldsymbol{\phi}_e, \qquad \nabla \phi = B_\phi \boldsymbol{\phi}_e. \tag{68}$$

Substitute the approximate solutions into the weak forms of the equations.

$$\begin{aligned} r_{\phi_2} = & \int_\Omega N_{\phi_2}^T N_{\phi_2} \dot{\phi_{2e}} \, dv \\ & - \frac{W^2}{\tau_0} \int_\Omega \Bigg[B_{\phi_2}^T B_{\phi_2} \phi_{2e} \\ & + N_{\phi_2}^T \left(-\frac{1}{W^2} \frac{\partial g(\phi_2)}{\partial \phi_2} \right) \\ & + N_{\phi_2}^T \left(\frac{a_1}{W\sigma} \frac{\partial p(\phi_2)}{\partial \phi_2} \Delta G_{ch} \right) \Bigg] \, dv, \end{aligned} \tag{69}$$

$$\begin{aligned} r_{c_A} = & \int_{\Omega_e} \dot{c}_A \, N_{c_A} \, dv \\ & + \int_{\Omega_e} \left[p(\phi_2) D_A^S B_{c_A} + (1 - p(\phi_2)) D_A^L B_{c_A} \right] \cdot B_{c_A} \, \mathbf{c}_A^e \, dv \\ & - \sum_{A=1}^N \int_{\Omega_e} \nabla \cdot \left[\sqrt{\frac{W}{2}} (N_{c_A} \mathbf{c}_A^e - c_A^L) \frac{\nabla \phi_2}{|\nabla \phi_2|} \frac{\partial \phi_2}{\partial t} \right] N_{c_A} \, dv = 0. \end{aligned} \tag{70}$$

3.2. Multi-scale multi-applications in MOOSE

The Multi-Application (MultiApp) system within MOOSE serves as a robust framework for conducting sophisticated multiscale simulations, where phenomena spanning different spatial and temporal scales are intricately interconnected. This framework allows for the seamless integration of multiple simulation modules, each dedicated to modeling specific aspects of a complex system. In the context of a melt pool simulation resulting from laser-induced heat transfer, the parent application primarily focuses on capturing the macroscopic behavior of the system. It simulates the thermal dynamics arising from the interaction between a laser heat source and the material, leading to the formation of a melt pool. Here, the parent application provides valuable insights into phenomena such as temperature distribution, heat fluxes, and melt pool morphology at a macroscopic level. However, to gain a comprehensive understanding of the underlying microstructural evolution within the melt pool, a more refined approach is necessary. This is where the MultiApp system proves invaluable. It facilitates the seamless transfer of critical information from the parent application to a sub-application specifically tailored for dendrite simulation. In the dendrite simulation sub-application, the focus shifts to modeling the microscale processes governing dendritic growth within the melt pool. This includes phenomena such as nucleation, growth, and coarsening of dendritic structures, which significantly influence the material's final microstructure and properties. By leveraging the MultiApp system, essential information such as temperature gradients, phase transitions obtained from the parent application can be seamlessly transferred to the dendrite simulation module. This enables a detailed exploration of microscale phenomena within the broader context of the melt pool simulation. Furthermore, the MultiApp system optimizes computational resources by enabling parallel execution of both the parent and sub-applications. This ensures efficient utilization of computing power, ultimately reducing simulation time and enhancing overall productivity. In summary, the MultiApp system facilitates the integration of parent and sub-applications in a hierarchical manner, enabling comprehensive multiscale simulations. By seamlessly coupling macroscopic and microscopic phenomena, it provides a holistic understanding of complex systems such as laser-induced melt pool formation and dendritic growth, thereby advancing our ability to predict and optimize material properties and manufacturing processes. Additionally, in scenarios where the sub-application domain represents an infinitesimally small portion of the parent application's domain, specialized Transfer mechanisms are utilized. For instance, "sampling" Transfers such as VariableValueSampleTransfer automatically evaluate single values from the parent app domain at sub-application positions, facilitating accurate data exchange. Conversely, postprocessor transfers play a crucial role in transmitting homogenized values from the sub-applications back to the parent application, ensuring seamless communication and enhancing the fidelity of multiscale simulations (see Algorithm 1).

Algorithm 1 Multi-Scale Multi-Applications in MOOSE Framework

```
Parent Application: Macroscale Melt Pool Simulation
Input: Laser heat source, material properties, process parameters
Output: Temperature distribution, heat fluxes, melt pool morphology
Steps:
1. Initialize the laser heat source, material domain, and boundary conditions.
2. Apply adaptive meshing for efficient heat transfer simulation.
3. Simulate heat transfer using the Transient Heat Conduction kernel.
4. Compute temperature gradients and heat fluxes using higher-order schemes.
5. Output melt pool morphology and thermal data.
Sub-Application: Microscale Dendrite Simulation
Input: Data from the parent application (temperature, phase transitions) and CALPHAD library (Python)
Output: Primary dendrite arm spacing (PDAS), microsegregation, crack initiation sites
Steps:
6. Initialize the microscale domain with a refined mesh.
7. Simulate dendritic growth using the Phase Field method.
8. Model undercooling and solute diffusion using CALPHAD thermodynamics.
9. Compute PDAS and microsegregation patterns using postprocessors.
10. Perform stress analysis to identify potential crack initiation sites.
11. Output microscale data for parent application feedback (optional).
```

4. Result and discussions

In this section, we present and discuss the simulation results obtained from a single-track simulation, demonstrating its reliability in effectively coupling temperature and phase-field formulations with mechanical responses. The results are compared with those provided by NIST for two different cases. The thermal response, which is influenced by mechanical effects and phase changes, is then transferred to the micro-phase-field model for a particular representative space to simulate dendrite growth in Ni-Nb-Al. The results are validated against the NIST benchmark. Finally, we focus on segregation evolution and the remaining liquid phase at the grain boundaries, which originates from the solidification rate driven by the cooling rate. The simulations are performed on a computer cluster equipped with two Intel CPUs (16 cores in total) and 128 GB of RAM. The CPU nodes are connected via a 40 Gbps InfiniBand network, enabling efficient communication between nodes and optimal utilization of parallel computing resources.

4.1. Material state variables in macro and micro phase field modeling

In Table 5, the parameters are referenced for macroscopic process modeling of the additive manufacturing (AM) process. The macroscopic material properties associated with temperature and phase parameters are detailed in Tables 6 and 7. In Table 6, the parameter φ denotes consolidation, serving as an indicator of phase to track the transformation of powder into the solid state. This parameter operates irreversibly, defined as $\varphi = \max\{\varphi(t), \varphi(t+dt)\}$, where it takes the maximum value of $\varphi(t)$ within two consecutive steps. This aligns with the principle that solidified material exists in a lower energy state compared to its liquid or powdered forms, making any return to a higher energy state thermodynamically unfavorable. Besides, the modeling parameters used for the microstructure evolution of a ternary system including Ni-Nb-Al are listed in Table 8.

Table 5
Phase field parameters for Inconel 625 [20].

Parameters	Value	Units
Kinetic coefficient (μ_ϕ)	0.5	mm K^{-1} s^{-1}
Interface width (δ)	1	mm
Surface tension (ω)	65×10^{-6}	mJ mm^{-2}
Latent heat (L)	23.8×10^{9}	mJ tonne^{-2}
Melting temperature (T_M)	1730	K

4.2. Melt pool size analysis

Our numerical investigation commenced with benchmark tests conducted under standardized and well-defined experimental conditions set forth by the National Institute of Standards and Technology (NIST). These conditions enable a direct comparison between experimental observations and results derived from numerical simulations of the process. To ensure concordance between the two, the simulation models underwent calibration, involving adjustments to various parameters and input values to closely align with the experimental data. This calibration process aimed to enhance the accuracy and reliability of the simulation results, ensuring a faithful representation of the physical phenomena inherent in the current additive manufacturing process. For the benchmark tests, we selected nickel-based superalloy 625 (IN625) substrates measuring 24.5 mm×4.5 mm, with a thickness of 3.2 mm. The powder utilized in these tests matched the material of the substrates. Specifically, we focused on a particular set of PBF experiments known as the “Additive Manufacturing Metrology Testbed” (AMMT) [47]. In this experimental setup, the laser size was reported as a 4-sigma diameter ($D4\sigma$) range of 170 μm, with a full-width half-maximum (FWHM) of 100 μm. For further details on the experimental setup, interested readers can refer to [48]. In our numerical simulations, we employed Goldak’s double-elliptical model for the heat source. The proposed numerical model, described in the preceding section, was simulated under two scenarios: Case B, with a laser power of 179.2 W and a scanning speed of 800 mm/s, and Case C, with a laser power of 179.2 W and a scanning speed of 1200 mm/s. As provided in Fig. 5, the surface topography of the tracks, provided by NIST, was measured and quantified using confocal laser scanning microscopy (CLSM), forming part of the Additive Manufacturing Benchmark Test Series (AM-Bench) [49]. Horizontal dashed lines in the figures indicate the estimated position of the original surface. The longitudinal profiles along the centerline of the tracks and the transverse profiles through the lowest point offer crucial insights. This information helps ensure that the morphology of the powder layer after deposition on the substrate is accurately represented. Comparing these results with simulations proposed here reveals that thermo-elastoplastic coupling can yield more efficient and accurate outcomes by capturing all effects in the AM process.

Then, to validate the results of the simulation with experiments robustly, the width of the laser tracks was determined *ex-situ* using CLSM and compared with the provided simulation outputs. Allied with this purpose, Fig. 7 depicts CLSM images of the laser track cross-sections corresponding to variations in laser power (P) and laser scan speed (V). It can be seen that the cross-section geometry was significantly influenced by both P and V [1]. Fig. 7 provides a transparent view of the evolution of powder consolidation for Case B, with dimensions of $2000 \times 800 \times 200\,\mu\text{m}^3$ over four-time steps. The thickness of the powder layer was considered to be 36 μm, following Lane et al. [47]. To capture the melt pool border, herein, AMR is implemented using a criterion based on gradient jumps in the phase-field variable at the molten and solidification frontiers. This method improves accuracy while ignoring the phase-field length value and minimum mesh size constraints. Fig. 6 shows the cross-sectional AMR area after the laser has passed.

Table 6
Material properties as a function of the phase-field parameter [20].

Material properties	Equations	Molten phase	Solidified phase
Thermal conductivity (κ) (W/mmk)	$\kappa(\varphi) = \phi\kappa_m + (1-\varphi)\kappa_d$	$\kappa_m = 30.25$	$\kappa_d = 11.10$
Specific heat capacity (c) (J/mm^3 k)	$c(\varphi) = \varphi c_m + (1-\varphi)c_d$	$c_m = 5.06$	$c_d = 3.30$
Thermal expansion (ξ) (1/K)	$\xi(\varphi) = \varphi\xi_m + (1-\varphi)\xi_d$	$\xi_m = 15 \times 10^{-6}$	$\xi_d = 10 \times 10^{-6}$
Young's modulus (E) GPa	$E(\varphi) = \varphi E_m + (1-\varphi)E_d$	$E_m = 85$	$E_d = 210$
Yield Stress (σ_Y) GPa	$\sigma_Y(\varphi) = \varphi\sigma_{Ym} + (1-\varphi)\sigma_{Yd}$	$\sigma_{Ym} = 0.03$	$\sigma_{Yd} = 0.24$

Table 7
Material properties as a function of the consolidation parameter [20].

Material properties	Equation	Molten phase	Solid phase
Density (ρ) (kg/mm^3)	$\rho(\varphi) = (1-\varphi)\rho_p + \varphi\rho_d$	$\rho_p = 4460$	$\rho_d = 7780$

Table 8
Equilibrium parameters utilized in the simulation. The equilibrium concentrations are obtained at $T_0 = 1362°\text{C}$, while other parameters represent average values within the solidification range of 1362°C to 1212°C. Concentration is expressed in units of mole fraction (m.f.) [46].

Parameter	Dimension	Nb	Al
$c^S_{\text{eq A}}(T_L)$	m.f.	0.0098	0.00505
$c^L_{\text{eq A}}(T_L)$	m.f.	0.051	0.005
$(c^S_{\text{eq}} - c^L_{\text{eq}})(T_L)$	m.f.	−0.0412	0.00005
$m^S_{A\phi_2}$	K/m.f.	−3640.8	3,700,000
$m^L_{A\phi_2}$	K/m.f.	−1468.7	330,000
$\chi^L_A \times 10^5$	J/mol@/m.f.	0.9	3.0
k^L_A	–	2.48	11.21
$m^L_A(T_0)$	K/m.f.	−1137.44	1.380
$D^L_A \times 10^{10}$	m^2/s	10.526	11.092

Algorithm 2 Mesh adaptivity algorithm for melt pool capturing

```
procedure MESH ADAPTIVITY
    Input:
        $marker(s)$
        $initial\_marker(s)$
        $max\_h\_level \leftarrow 2$
    Configuration of Indicators:
        $Indicators/indicator$
            $type \leftarrow$ GradientJumpIndicator
            $variable \leftarrow \phi$
    Configuration of Markers:
        $Markers/marker$
            $type \leftarrow$ ErrorFractionMarker
            $indicator \leftarrow$ indicator
            $coarsen \leftarrow 0.3$
            $refine \leftarrow 0.7$
end procedure
```

As illustrated in Figs. 7(b) and 7(e), the respective samples were cross-sectioned perpendicular to the laser moving path. Following this, standard metallurgical sample preparation techniques, including mounting and polishing, were utilized to facilitate comparison with the overall shape of the modeled melt pools. This method allows for a qualitative evaluation of how well the simulated melt pool aligns with the actual physical samples obtained through cross-sectioning and sample preparation. Notably, a close agreement between the simulation results in Figs. 7(d) and 7(g) and the experimental measurements obtained from the AMMT samples [49] was observed, as indicated in Table 9. The computational time for both cases is presented using the AMR technique.

4.3. Solidification parameters

Table 9
Comparison between numerical simulation [20] and experimental data benchmarked by NIST [49,50].

AMMT Melt Pool Dimensions	Case B	Case C
Average Width by NIST (μm)	123.46	106.02
Width by PF-AC (μm)	116.83	102.96
Average Depth by NIST (μm)	35.96	29.15
Depth by PF-AC (μm)	45.53	39.61
CPU-wall time (s)	314	418

Dendrite morphology, particularly the primary dendrite arm spacing (PDAS), serves as a key microstructural indicator in AM processes. PDAS is often associated with parameters like temperature gradient (G), solidification velocity (V_c), and cooling rate (R), as shown in Eq. (71):

$$(G, V_c, R) = \left(\sqrt{\left(\frac{\partial T}{\partial x}\right)^2 + \left(\frac{\partial T}{\partial y}\right)^2 + \left(\frac{\partial T}{\partial z}\right)^2}, \frac{dT}{dt}, \frac{V_c}{G} \right) \tag{71}$$

As illustrated in Fig. 8, the solidification pattern is determined by these parameters. The ratio of G to R, denoted as G/R, plays a crucial role in shaping the solidification microstructure, resulting in various morphologies such as planar, cellular, columnar dendritic, and equiaxed dendritic structures. The cooling rate directly affects the size of the microstructure, with higher cooling rates leading to finer microstructures. Under rapid solidification conditions present in PBF, a power-law relationship for the dendrite arm spacing, $\Lambda \propto R^{-a}$, with a scaling factor of 0.56–0.57 has been reported, slightly higher than traditional directional solidification [51]. PDAS evaluation methods, such as Kurz-Fisher's or Hunt's models, typically show a linear relationship with $G^{-0.5}V_c^{-0.25}$. These phenomena significantly influence the material's microstructure and mechanical properties, ultimately impacting the overall performance and quality of manufactured components. Therefore, precise control of the cooling rate is essential for achieving desired material properties and ensuring the success of additive manufacturing processes.

Fig. 9 demonstrates diagrams that provide insights into the interplay between process parameters and melt pool dimensions, as well as solidification characteristics. It is evident that increasing laser power results in a reduction in both the depth and width of the melt pool, leading to lower temperature gradients and smaller melt pools size. Conversely, the effect of scanning speed is opposite: as laser power increases, the depth and width of the melt pool decrease, while the temperature gradient increases. The parameter G/R, indicative of dendrite microstructure, decreases with increasing laser power and scanning speed. Consequently, an increase in this parameter suggests a transition towards a planar structure, whereas a decrease indicates the likelihood of an equiaxed structure. PDAS analysis reveals that both increasing laser power and scanning speed tend to increase PDAS. However, when laser power increases while scanning speed remains constant, the dendrite arm spacing tends to decrease, resulting in finer microstructures. This intricate relationship underscores the importance of carefully controlling process parameters to achieve desired microstructural characteristics in additive manufacturing. To assess the accuracy of our simulation, we selected the case presented in Fig. 7, which was

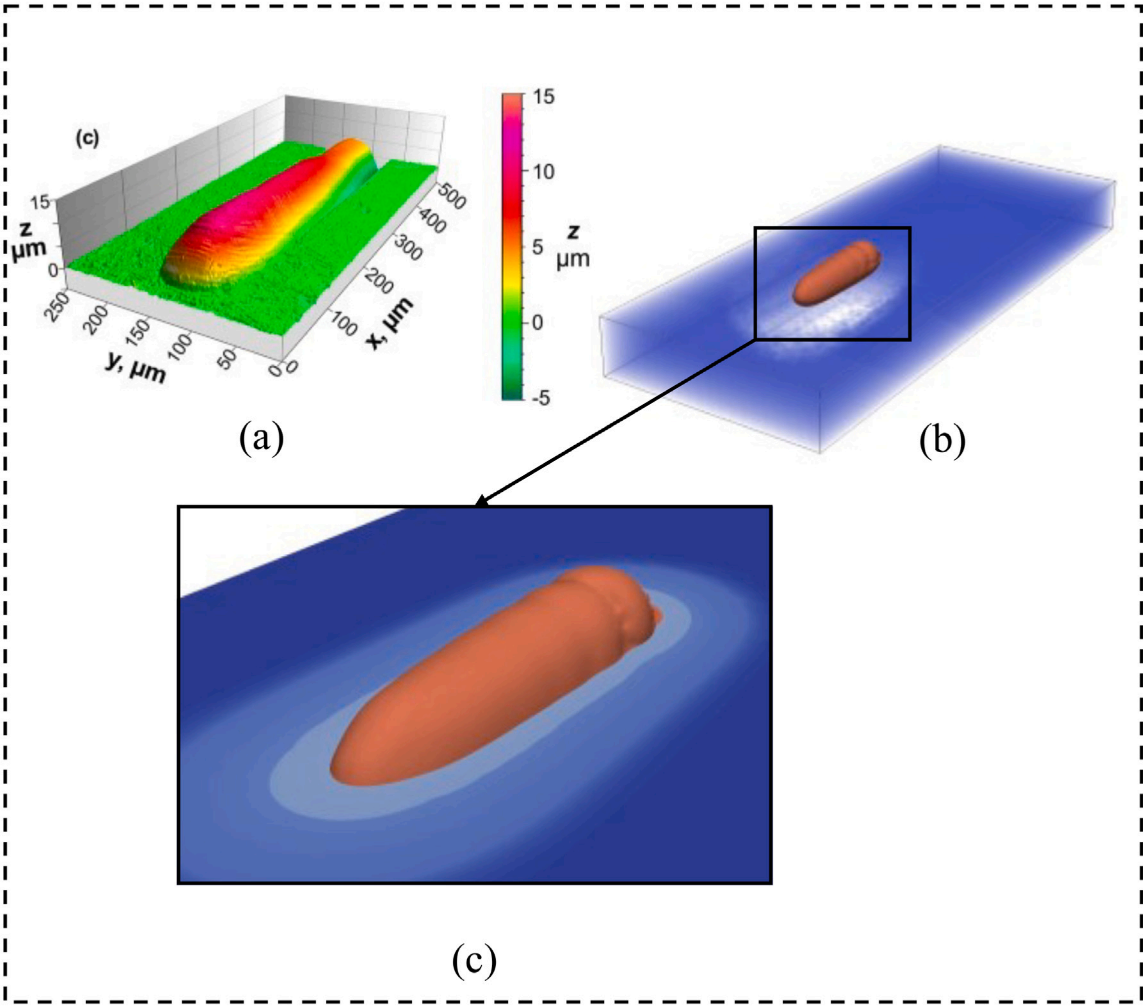

Fig. 5. Pseudo-color 3D height maps of the start and end of tracks created in the AMMT: (a): Case B from [49], (b): Simulation results of the same case study on the top of the substrate, (c): Enlarged view of the PBF-deposited line.

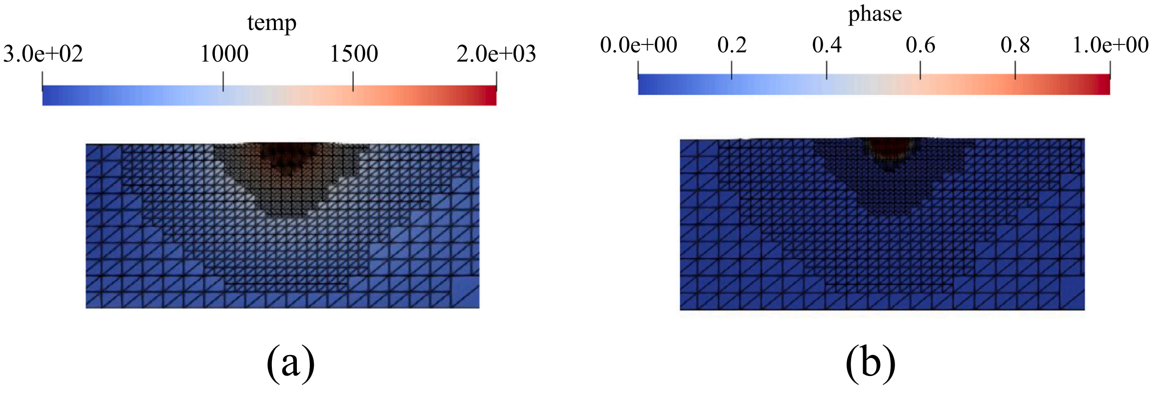

Fig. 6. Cross-sectional view of the melt pool with AMR in Case B: 179.2 W, 800 mm/s (AMMT) adapted from Heigel et al. [48], (a): temperature distribution, (b): phase evolution.

previously compared in terms of melt pool size to evaluate solidification parameters. This comparison provides crucial information for the subsequent section, where we calculate cellular dendrite patterns using micro phase-field modeling (Section 4.4). Table 10 demonstrates a good agreement between the simulation and experimental results.

4.4. Cellular solidification and microsegregation characteristics

The phase-field simulations were conducted within a 2D computational space measuring $10 \times 20\,\mu\text{m}^2$. Boundary conditions were set to zero-flux for all fields except for a constant concentration c_0 at the

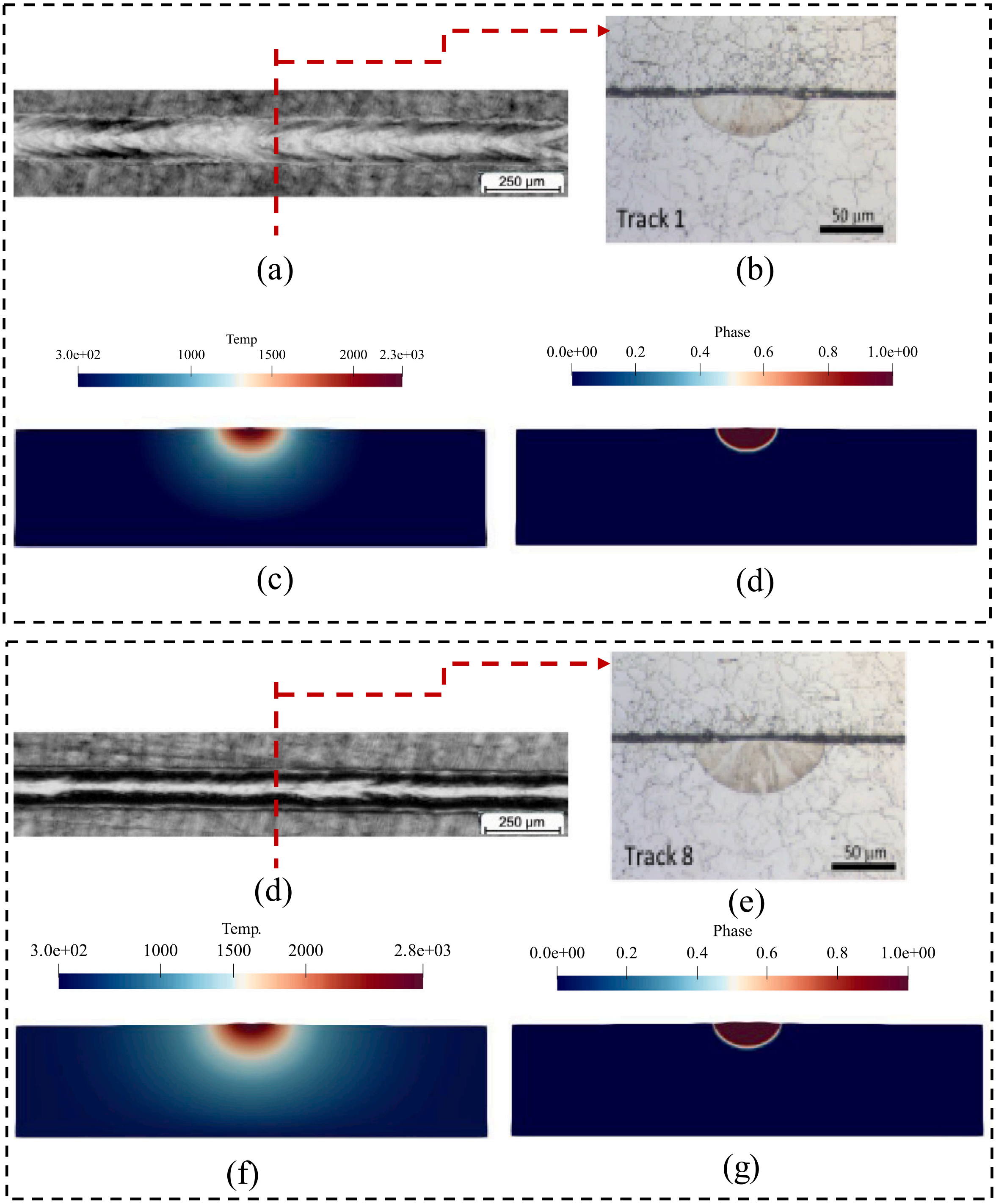

Fig. 7. Simulation results of Case B: 179.2 W, 800 mm/s (AMMT), (a): Experimental single line, (b): cross-sectional adapted from Heigel et al. [48] (c): Cross-sectional temperature, (d): phase field variable. Simulation results of Case C: 179.2 W, 1200 mm/s (AMMT), (a): Experimental single line, (b): cross-sectional adapted from Heigel et al. [48] (c): Cross-sectional temperature, (d): phase field variable. Note: All temperatures are in Kelvin degree.

Table 10
Comparison of Case 3: NIST vs. PF-AC Simulation.

	NIST	PF Simulation	Deviation (%)
G (K/m)	1.2×10^7	11.46×10^6	4.5%
R (m/s)	0.1	0.094	6%

upper boundary. To discretize the domain effectively, a grid spacing of $dx = dz = 0.25\,\mu\mathrm{m}$ was employed, ensuring high resolution. Time increments were set at $dt = 0.04\tau_0$, utilizing a characteristic time scale τ_0. To accurately represent the interface between solid and liquid phases, an interface thickness of 15 nm (W) was chosen, considerably smaller than typical microstructure dimensions. Initialization involved introducing randomly distributed nuclei at the domain's bottom, while the concentration field was set to $c_s^{eq}(T_L)$ in the solid phase and $c_l^{eq}(T_L)$ in the liquid phase, where T_L represents the liquidus temperature. Stochastic effects were introduced through Langevin noise in Eq. (47), creating fluctuations at the interface during microstructure evolution to capture the inherent randomness of solidification processes [53].

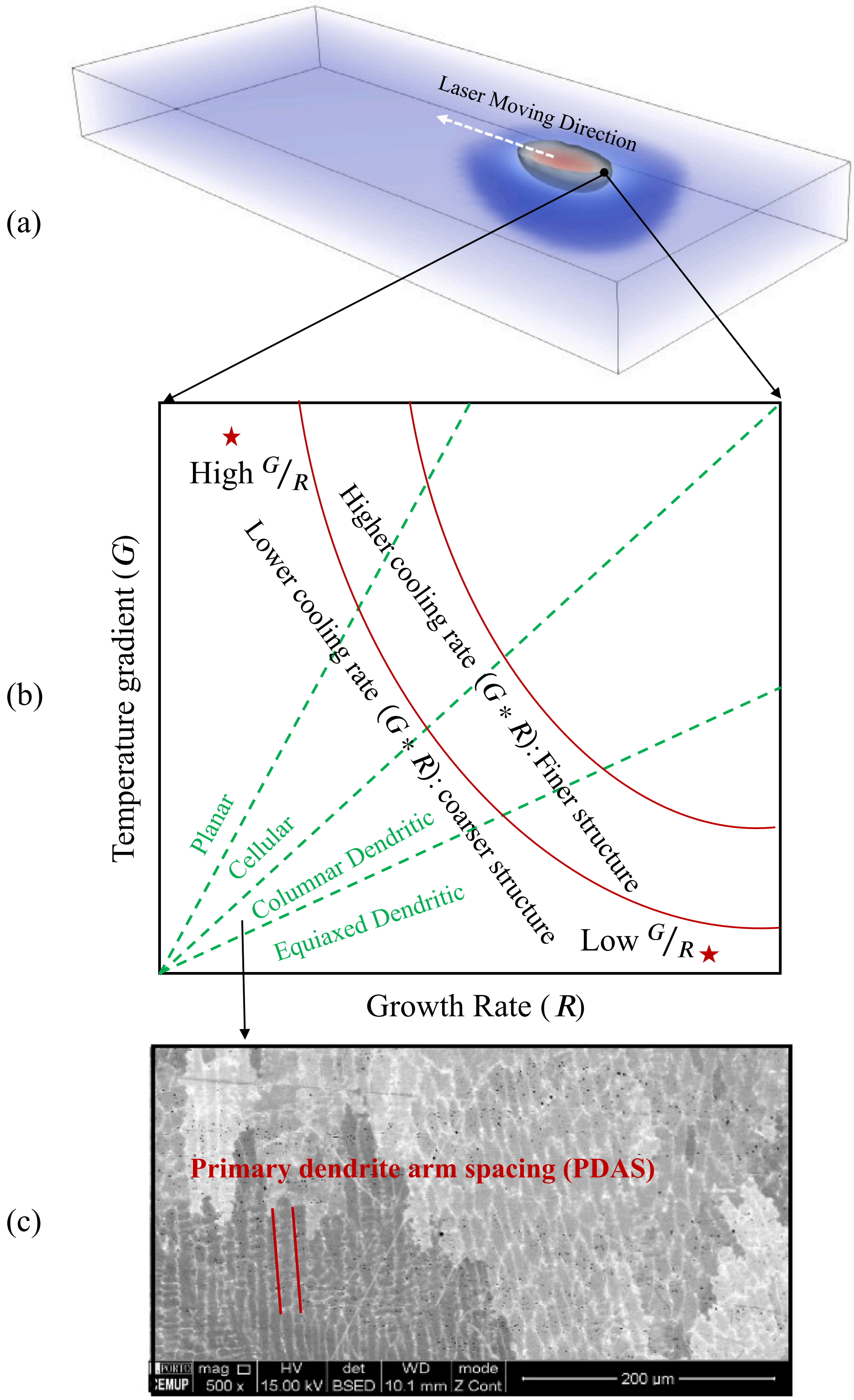

Fig. 8. Schematic illustrating the thermal influence on dendritic microstructure, (a): Transient melt pool tail, (b): Influence of temperature gradient and growth rate on grain structure pattern, (c): Primary arm spacing dendrite on a printed sample using process parameters including laser power = 1.8 kW, scanning speed = 6 mm/s, and feed rate = 12 g/min. [52].

Thermodynamic properties were obtained from prior studies to ensure consistency, providing essential inputs for accurately modeling the solidification behavior of the Ni-Nb-Al alloy system [23,24]. The feasibility of the proposed PF model is initially assessed under specific thermal conditions typical of LPBF processing. These conditions include a cooling rate of 1.2×10^6 K/s and a temperature gradient of 1.2×10^7 K/m, falling within the range of reasonable thermal variables during LPBF, as outlined in Table 10. Fig. 2(a) illustrates the simulated temporal evolution of microstructures, revealing the emergence of cellular structures within LPBF-built components. These structures are visualized through variations in Nb and Al concentrations. Fig. 11 showcases snapshots of a typical cellular microstructure during the

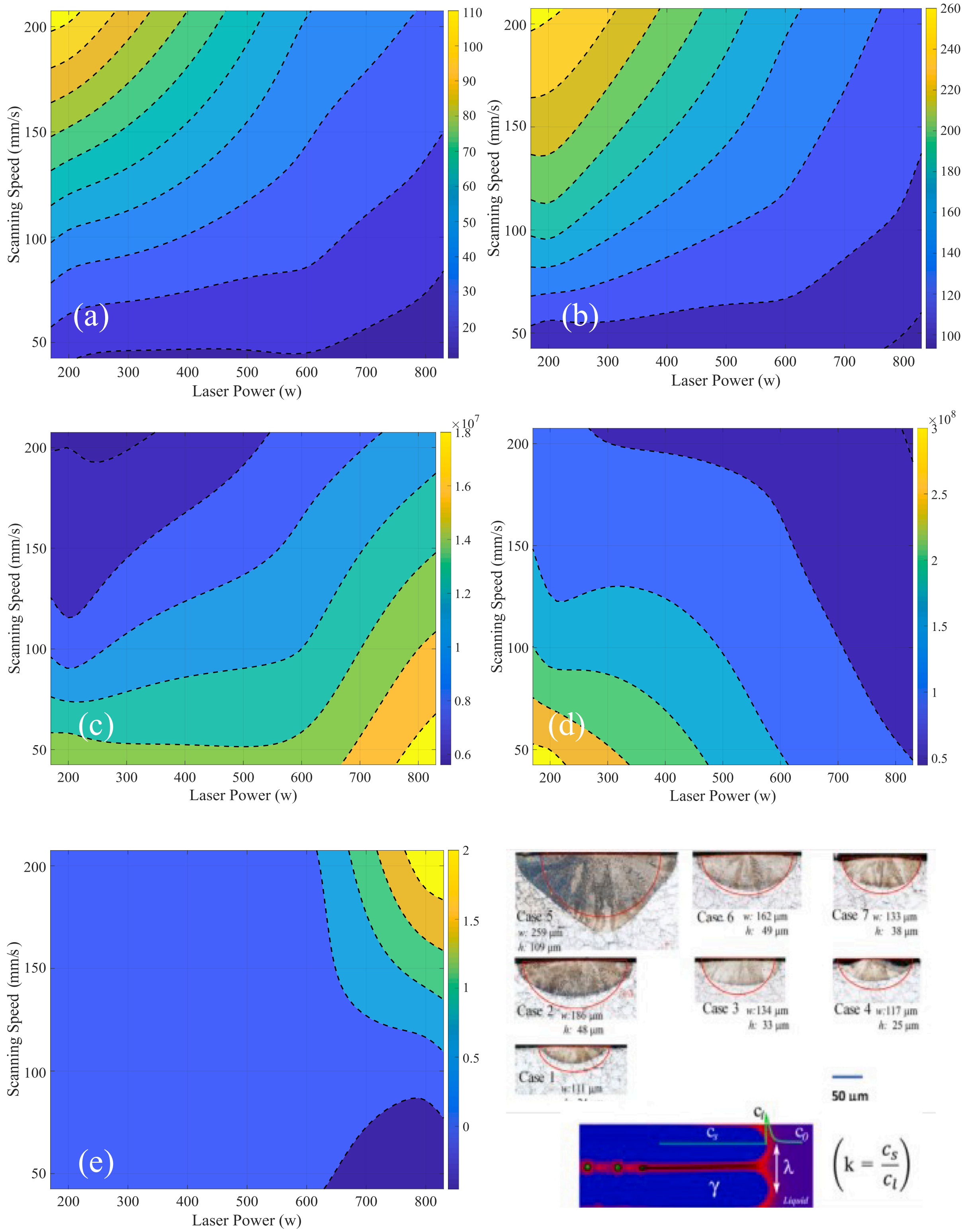

Fig. 9. (a, b): Contours representing melt pool dimensions (depth and width in microns) observed from transverse cross-sections of laser tracks [49]. (c): Temperature gradient (K/m) under various printing conditions. (d): Ratio G/R (K/s) as a parameter indicating dendritic microstructure. (e): Primary Dendrite Arm Spacing (PDAS) size in microns for different deposition conditions after solidification. (f, g): Schematic cross-sectional view and measured parameters for PDAS size in microns [49].

rapid cooling stage, corresponding to a laser power of 195 W and a scanning velocity of 800 mm/s. These snapshots provide visual representation of the solidification process, which is further elaborated upon in Table 10. Specifically, in Fig. 11 ($a_1 - a_3$), the evolution of non-conserved parameters governing the movement of the solidification boundary is depicted across three distinct time stages, ranging from 4 ms to 40 ms. Additionally, Fig. 11 ($b_1 - b_3$) illustrates the concentration of Nb within the Ni matrix, highlighting maximum values at the solidification boundary, denoted as c_l (17.3%) and c_s (19.6%), with a nominal composition of c_0 (20.28%). Then, in Fig. 11 ($c_1 - c_3$), the concentration of Al inside the Ni matrix is shown in the same time interval with c_l (0.48%) and c_s (0.51%), with a nominal composition

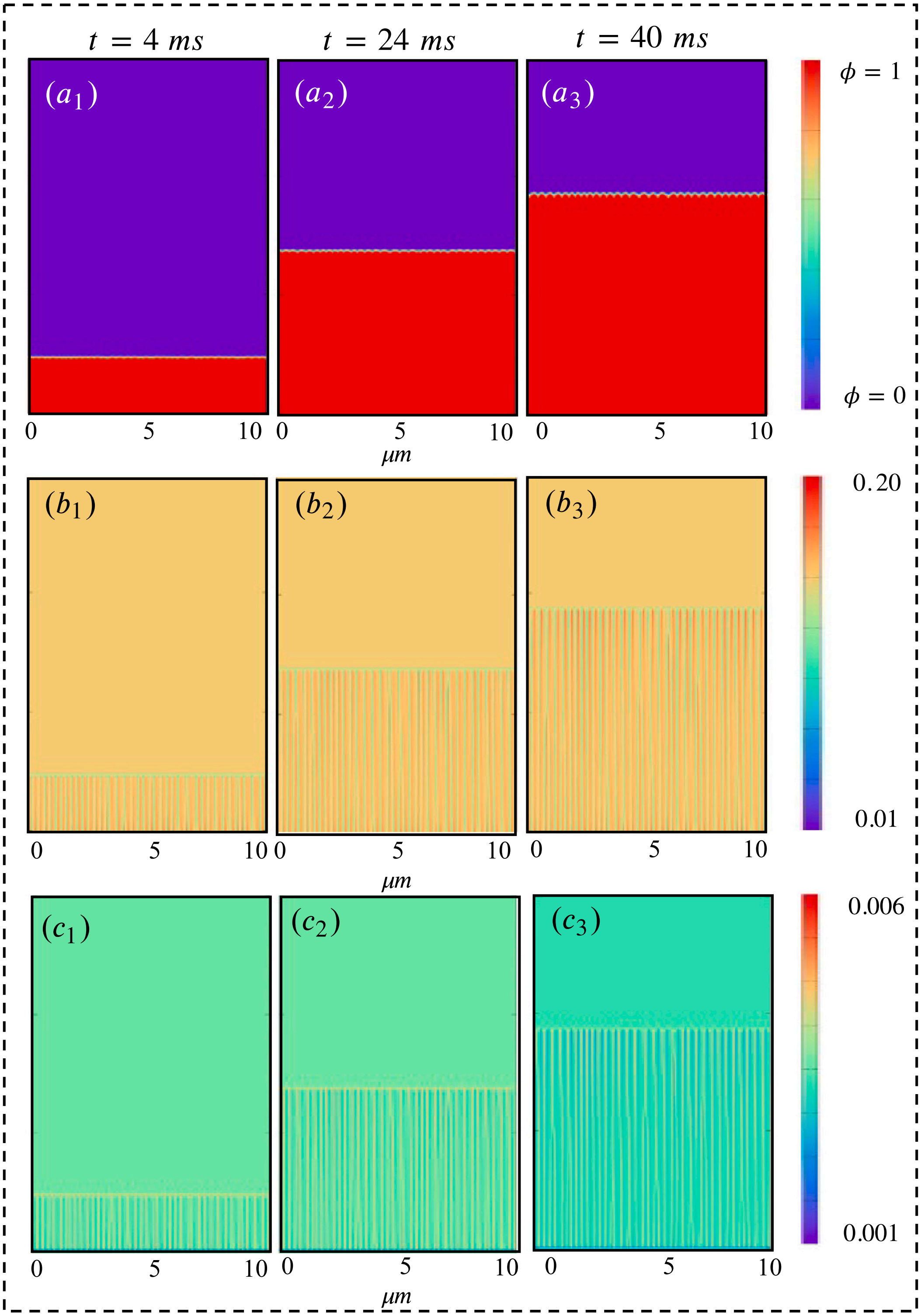

Fig. 10. Simulation results of rapid solidification in Ni-Nb-Al with a cooling rate of 6×10^6 K/s and a temperature gradient of 1.2×10^7 K/s. Panels (a1-a3): Evolution of solidification front and order parameter. Panels (b1-b3): Evolution of cellular structure at different solidification times, depicted by solute concentration (at.% Nb).

of c_0 (0.58%) is illustrated. Initially, as solidification commences and initial nuclei begin to grow, solute rejection occurs, leading to the accumulation of solute at the solid–liquid interface due to differing solute diffusivities in the solid and liquid phases. Consequently, the liquidus temperature fluctuates at the interface, inducing local perturbations or instabilities. These instabilities are subsequently amplified, evolving into protrusions along the direction of the temperature gradient. As the microstructure evolves further, solutes rejected laterally by these protrusions impede the growth of regions between them, ultimately giving rise to the formation of the initial cellular structure. In order to conduct these simulations, material properties and modeling parameters were meticulously specified and detailed, as presented in Table 8. This table serves as a comprehensive reference for the simulation setup, providing insight into the parameters utilized throughout the study. The calculated and simulated values of the conserved parameter Nb, serving as the PASD, are compared with NIST benchmarks in

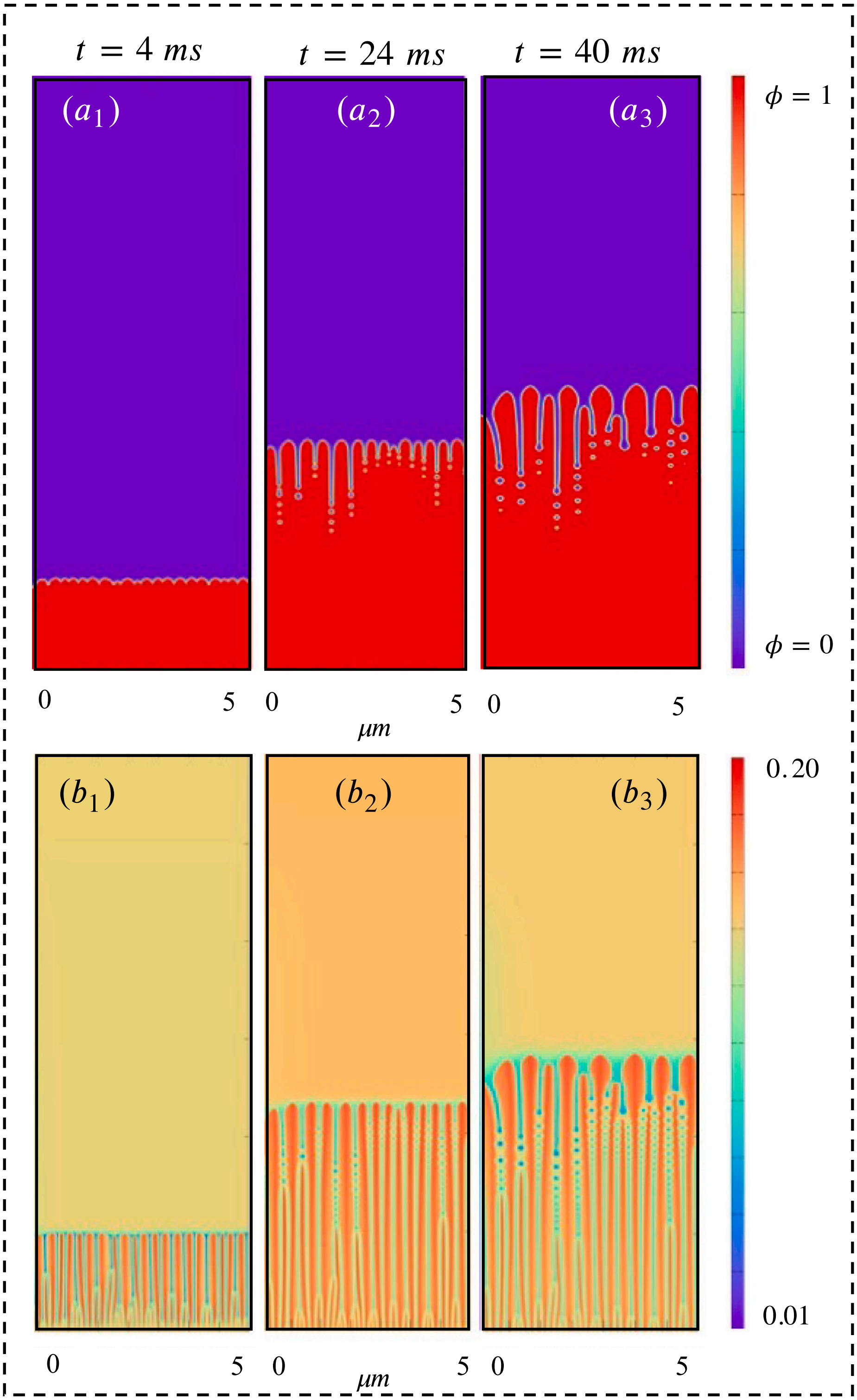

Fig. 11. Microstructure evolution during rapid solidification for Case B: 179.2 W, 800 mm/s (AMMT) in [48–50] of Ni-Nb-Al at a cooling rate of 11.46×10^6 K/s and a temperature gradient of 1.2×10^7 K/m. $(a_1 - a_3)$: Evolution of solidification frontier and order parameter. $(b_1 - b_3)$: Evolution of cellular structure at different solidification times, represented by solute concentration (at.% Nb). $(c_1 - c_3)$: Evolution of cellular structure at different solidification times, represented by solute concentration (at.% Al).

Table 11. The comparison highlights the strong agreement between the microstructure PF simulation and the experimental data provided by [49]. Moreover, the simulation took 3 h and 24 min using the aforementioned computational resources.

To investigate the impact of cooling rate, a critical factor in microstructure simulation and the occurrence of defects like liquation pockets and solidification cracks, we compared the results of micro PF simulations with those provided by NIST in Fig. 11. A significantly higher cooling rate, five times greater, was chosen for the simulation as shown in Fig. 10 in the smaller spatial discretization including 5 μm × 20 μm. In LPBF processes, rapid solidification occurs due to high cooling rates, allowing limited time for solute atoms to diffuse within the solidifying material. This rapid solidification often results in the formation of liquation pockets, particularly evident in alloy systems like Ni-Nb-Al,

Table 11
Comparison of Case 3: NIST [49] vs. PF Simulation in PASD size and concentration of Nb.

	NIST	PF Simulation	Deviation (%)
G (K/m)	1.2×10^7	11.46×10^6	4.5%
R (m/s)	0.1	0.094	6%
λ (μm)	0.35	0.3125	10.7%
k (Nb)	0.64	0.42	34.4%

where certain elements, such as Nb, have limited solubility in the solid phase at lower temperatures(see Fig. 10 ($a_1 - a_3$)). Liquation pockets arise from the segregation of solute elements at grain boundaries (GB) or within the microstructure, driven by the rapid cooling and solidification process. The insufficient diffusion of solute atoms during the short solidification period leads to the localized enrichment of elements like Nb, forming liquation pockets within the solidified structure. The presence of liquation pockets introduces areas of localized stress concentration within the material. Under conditions of thermal cycling or mechanical loading, these stress concentrations act as preferential sites for crack initiation. Moreover, the compositional variation introduced by liquation pockets can disrupt the normal solidification process, leading to incomplete bonding between successive layers or incomplete filling of the melt pool. It can be said that the combination of rapid solidification and liquation pocket formation increases the likelihood of porosity and crack formation in the final solidified part. Therefore, controlling the cooling rate is crucial for minimizing microstructural defects and ensuring the structural integrity of components produced through LPBF processes. Herein, the simulation took 1 h and 17 min using the aforementioned computational resources.

5. Conclusions

In conclusion, this study presents a comprehensive thermomechanical simulation framework for powder bed fusion (PBF) processes, with a particular emphasis on melt pool characterization, initially using the macro-phase field model. By integrating the Allen-Cahn phase-field formulation with a thermal elastoplastic material model based on J2 plasticity theory, our computational framework, implemented within the MOOSE finite element structure, enables precise simulations of melt pool behavior. Through rigorous evaluations — including three-dimensional simulations of Inconel 625 thin plates and benchmark examples — we have analyzed the impact of key process parameters, such as temperature variations and phase transitions, on melt pool dimensions. Despite the strengths of this multiphysics modeling framework, one of its primary limitations is the exclusion of fluid flow effects, including melt pool convection, surface tension-driven Marangoni flow, and recoil pressure. Instead, a conduction-driven melt pool shape is assumed, which, while sufficient for solidification-driven microstructure evolution, does not capture convective instabilities. Nonetheless, validation through single-track laser melting experiments and simulations on Inconel 625 has demonstrated a strong correlation between experimental and computational results, confirming the robustness of our approach. Building upon this macro-phase field model, our study further implements a micro-phase field model to address critical challenges related to parameter interplay, defect detection, and liquation cracking within PBF processes. By linking thermal evolution from the macro-phase field model to the CALPHAD library, we provide insights into the influence of process parameters on primary dendrite arm spacing (PDAS). Additionally, we introduce a novel dendrite modeling approach using a dedicated sub-application for surrogate Ni-Nb-Al ternary systems, where the melt pool boundary serves as a critical point in a 2D representative space. This integrated CALPHAD-based approach enables the transfer of critical solidification parameters, such as temperature gradients and cooling velocities, enhancing our understanding of liquation crack formation due to low-melting phases. It is worth noting that this level of implementation has also been conducted within the MOOSE framework. Furthermore, micro-phase field simulations predict the size and segregation of cellular microstructures along melt pool boundaries under varying solidification conditions, establishing direct correlations between melt pool dimensions, cooling rates, PDAS, and segregation patterns. However, the micro-phase field model, while efficiently implemented in a refined 2D simulation space, does not fully account for three-dimensional solidification kinetics, potentially limiting its predictive accuracy for complex dendritic morphologies. To further validate our formulation, simulation results are compared with the NIST benchmark for PDAS, demonstrating its capability to account for ternary models instead of full alloy element effects. Overall, this study makes a significant contribution to the understanding of PBF and additive manufacturing (AM) processes, offering practical insights for optimizing production outcomes. By addressing challenges in dendrite modeling and liquation crack prediction for alloy systems under diverse cooling conditions, our research advances AM technology and its industrial applications.

These findings have the potential to enhance the quality of AM-produced components, reduce material waste, and improve the reliability of AM for high-performance applications in industries such as aerospace and energy. As a future research direction, we aim to develop a reinforcement learning framework that leverages iterative process data to enable real-time control of process parameters. This approach aspires to achieve in-situ defect mitigation and predictive microstructure control, ultimately working towards an “utopia scenario” in PBF-based additive manufacturing.

CRediT authorship contribution statement

Roya Darabi: Writing – original draft, Software, Methodology, Data curation, Conceptualization. **João Pedro Oliveira:** Writing – review & editing, Validation, Formal analysis, Data curation. **Narguess Nemati:** Writing – review & editing, Validation, Formal analysis. **Ana Reis:** Writing – review & editing, Supervision, Investigation, Data curation. **Jose Cesar de Sá:** Writing – review & editing, Visualization, Validation, Investigation.

Funding

R. Darabi gratefully acknowledges the funding of the project Hi-rEV – Recuperação do Setor de Componentes Automóveis under the program PRR - Plano de Recuperação e Resiliência - Agendas Mobilizadoras funded by Agência para a Competitividade e Inovação, Portugal.

Declaration of competing interest

The authors declare that they have no known competing financial interests or personal relationships that could have appeared to influence the work reported in this paper.

Data availability

The data that support the findings of this study are available from the corresponding author upon reasonable request.

References

[1] Zhengtao Gan, Yanping Lian, Stephen E. Lin, Kevontrez K. Jones, Wing Kam Liu, Gregory J. Wagner, Benchmark study of thermal behavior, surface topography, and dendritic microstructure in selective laser melting of inconel 625, Integr. Mater. Manuf. Innov. 8 (2) (2019) 178–193.

[2] Jianjun Xu, Xin Lin, Pengfei Guo, Hongbiao Dong, Xiaoli Wen, Qiuge Li, Lei Xue, Weidong Huang, The initiation and propagation mechanism of the overlapping zone cracking during laser solid forming of in-738lc superalloy, J. Alloys Compd. 749 (2018) 859–870.

[3] Yuanbo T. Tang, Chinnapat Panwisawas, Joseph N. Ghoussoub, Yilun Gong, John W.G. Clark, André A.N. Németh, D. Graham Mccartney, Roger C. Reed, Alloys-by-design: Application to new superalloys for additive manufacturing, Acta Mater. 202 (2021) 417–436.

[4] V.D. Divya, R. Muñoz-Moreno, O.M.D.M. Messé, J.S. Barnard, S. Baker, T. Illston, H.J. Stone, Microstructure of selective laser melted cm247lc nickel-based superalloy and its evolution through heat treatment, Mater. Charact. 114 (2016) 62–74.

[5] Qingsong Wei, Yin Xie, Qing Teng, Muyu Shen, Shanshan Sun, Chao Cai, Crack types, mechanisms, and suppression methods during high-energy beam additive manufacturing of nickel-based superalloys: A review, Chin. J. Mech. Engineering: Addit. Manuf. Front. 1 (4) (2022) 100055.

[6] O. Hunziker David Dye, Roger C. Reed, Numerical analysis of the weldability of superalloys, Acta Mater. 49 (4) (2001) 683–697.

[7] Michael Cloots, Peter J. Uggowitzer, Konrad Wegener, Investigations on the microstructure and crack formation of in738lc samples processed by selective laser melting using Gaussian and doughnut profiles, Mater. Des. 89 (2016) 770–784.

[8] Quanquan Han, Yuchen Gu, Shwe Soe, Franck Lacan, Rossitza Setchi, Effect of hot cracking on the mechanical properties of hastelloy X superalloy fabricated by laser powder bed fusion additive manufacturing, Opt. Laser Technol. 124 (2020) 105984.

[9] Hongyu Wu, Dong Zhang, Biaobiao Yang, Chao Chen, Yunping Li, Kechao Zhou, Liang Jiang, Ruiping Liu, Microstructural evolution and defect formation in a powder metallurgy Nickel-based superalloy processed by selective laser melting, J. Mater. Sci. Technol. 36 (2020) 7–17.

[10] Joel Andersson, Welding metallurgy and weldability of superalloys, Metals 10 (1) (2020).

[11] Afolabi T. Egbewande, R.A. Buckson, Olanrewaju A. Ojo, Analysis of laser beam weldability of inconel 738 superalloy, Mater. Charact. 61 (5) (2010) 569–574.

[12] Yuan Chen, Ke Zhang, Jian Huang, Seyed Reza Elmi Hosseini, Zhuguo Li, Characterization of heat affected zone liquation cracking in laser additive manufacturing of inconel 718, Mater. Des. 90 (2016) 586–594.

[13] Yao Li, Kai Chen, Nobumichi Tamura, Mechanism of heat affected zone cracking in Ni-based superalloy Dz125L fabricated by laser 3D printing technique, Mater. Des. 150 (2018) 171–181.

[14] M.B. Henderson, D. Arrell, R. Larsson, M. Heobel, G. Marchant, Nickel based superalloy welding practices for industrial gas turbine applications, Sci. Technol. Weld. Join. 9 (1) (2004) 13–21.

[15] Duy Nghia Luu, Wei Zhou, Sharon Mui Ling Nai, Mitigation of liquation cracking in selective laser melted inconel 718 through optimization of layer thickness and laser energy density, J. Mater. Process. Technol. 299 (2022) 117374.

[16] Ranadip Acharya, John A. Sharon, Alexander Staroselsky, Prediction of microstructure in laser powder bed fusion process, Acta Mater. 124 (2017) 360–371.

[17] Trevor Keller, Greta Lindwall, Supriyo Ghosh, Li Ma, Brandon M. Lane, Fan Zhang, Ursula R. Kattner, Eric A. Lass, Jarred C. Heigel, Yaakov Idell, Maureen E. Williams, Andrew J. Allen, Jonathan E. Guyer, Lyle E. Levine, Application of finite element, phase-field, and calphad-based methods to additive manufacturing of Ni-based superalloys, Acta Mater. 139 (2017) 244–253.

[18] Jinhu Zhang, Xuexiong Li, Dongsheng Xu, Chunyu Teng, Hao Wang, Phase field simulation of the stress-induced α microstructure in ti – 6al – 4 V alloy and its Cpfem properties evaluation, J. Mater. Sci. Technol. 90 (2021) 168–182.

[19] Derek Gaston, Chris Newman, Glen Hansen, Damien Lebrun-Grandié, Moose: A parallel computational framework for coupled systems of nonlinear equations, Nucl. Eng. Des. 239 (10) (2009) 1768–1778.

[20] Roya Darabi, Erfan Azinpour, Ana Reis, Jose Cesar De Sa, Multi-scale multi-physics phase-field coupled thermo-mechanical approach for modeling of powder bed fusion process, Appl. Math. Model. 122 (2023) 572–597.

[21] Cody J. Permann, Derek R. Gaston, David Andrš, Robert W. Carlsen, Fande Kong, Alexander D. Lindsay, Jason M. Miller, John W. Peterson, Andrew E. Slaughter, Roy H. Stogner, Richard C. Martineau, Moose: Enabling massively parallel multiphysics simulation, Softwarex 11 (2020) 100430.

[22] Alexander D. Lindsay, Derek R. Gaston, Cody J. Permann, Jason M. Miller, David Andrš, Andrew E. Slaughter, Fande Kong, Joshua Hansel, Robert W. Carlsen, Casey Icenhour, Logan Harbour, Guillaume L. Giudicelli, Roy H. Stogner, Peter German, Jacob Badger, Sudipta Biswas, Leora Chapuis, Christopher Green, Jason Hales, Tianchen Hu, Wen Jiang, Yeon Sang Jung, Christopher Matthews, Yinbin Miao, April Novak, John W. Peterson, Zachary M. Prince, Andrea Rovinelli, Sebastian Schunert, Daniel Schwen, Benjamin W. Spencer, Swetha Veeraraghavan, Antonio Recuero, Dewen Yushu, Yaqi Wang, Andy Wilkins, Christopher Wong, 2.0 - moose: Enabling massively parallel multiphysics simulation, Softwarex 20 (2022) 101202.

[23] Yong Du, Y.A. Chang, Weiping Gong, Baiyun Huang, Honghui Xu, Zhanpeng Jin, F. Zhang, S.L. Chen, Thermodynamic properties of the Al-Nb-Ni system, Intermetallics 11 (10) (2003) 995–1013.

[24] Fan Zhang, Ni-Nb-Al pseudo-ternary thermodynamic database, Madison, Wi, 2010 (2010).

[25] Fadi Aldakheel, Mechanics Of Nonlocal Dissipative Solids : Gradient Plasticity and Phase Field Modeling Of Ductile Fracture Mechanics Of Nonlocal Dissipative Solids : Gradient Plasticity and Phase Field Modeling Of Ductile Fracture, vol. 34, 2016, p. 160.

[26] Fadi Aldakheel, Micromorphic approach for gradient-extended thermo-elastic–plastic solids in the logarithmic strain space, Contin. Mech. Thermodyn. 29 (6) (2017) 1207–1217.

[27] Baharin Ali, Yousef Heider, Bernd Markert, Residual stresses in gas tungsten arc welding : A novel phase-field thermo-elastoplasticity modeling and parameter treatment framework, Comput. Mech. 69 (2) (2022) 565–587.

[28] Juan C. Simo, Christian Miehe, Associative coupled thermoplasticity at finite strains: Formulation, numerical analysis and implementation, Comput. Methods Appl. Mech. Engrg. 98 (1) (1992) 41–104.

[29] Erfan Azinpour, Roya Darabi, Jose Cesar De Sa, Abel Santos, Josef Hodek, Jan Dzugan, Fracture analysis in directed energy deposition (Ded) manufactured 316L stainless steel using a phase-field approach, Finite Elem. Anal. Des. 177 (2020) 103417.

[30] Erfan Azinpour, Daniel Melzer Sylwia Rzepa, Ana Reis, J Jan ZUgan, Jose Manuel Cesar de Sa, Phase-field ductile fracture analysis of multi-materials and functionally graded composites through numerical and experimental methods, Theor. Appl. Fract. Mech. 125 (2023) 103906.

[31] Long Qing Chen, Yuhong Zhao, From classical thermodynamics to phase-field method, Prog. Mater. Sci. 124 (2022) 100868.

[32] Dominic G.B. Edelen, Primitive thermodynamics: A new look at the Clausius-Duhem inequality, Internat. J. Engrg. Sci. 12 (2) (1974) 121–141.

[33] Bernard D. Coleman, Walter Noll, The thermodynamics of elastic materials with heat conduction and viscosity, Arch. Ration. Mech. Anal. 13 (1) (1963) 167–178.

[34] William Boettinger, James A. Warren, Christoph Beckermann, Alain Karma, Phase-field simulation of solidification, in: Annual Review of Materials Science, vol. 32, 2002, pp. 163–194.

[35] Samuel Miller, John Werner Cahn, Ground state structures in ordered binary alloys with second neighbor interactions, Acta Metall. 20 (3) (1972) 423–433.

[36] J.Y. Shanghvi, P. Michaleris, Thermo-elasto-plastic finite element analysis of quasi-state processes in Eulerian reference frames, Internat. J. Numer. Methods Engrg. 53 (7) (2002) 1533–1556.

[37] Seong Gyoon Kim, A phase-field model with antitrapping current for multicomponent alloys with arbitrary thermodynamic properties, Acta Mater. 55 (13) (2007) 4391–4399.

[38] Julia Kundin, Leslie Mushongera, Heike Emmerich, Acta materialia phase-field modeling of microstructure formation during rapid solidification in inconel 718 superalloy, Acta Mater. 95 (2015) 343–356.

[39] Balasubramaniam Radhakrishnan, Sarma B. Gorti, John A. Turner, Ranadip Acharya, John A. Sharon, Alexander Staroselsky, Tahany El-Wardany, Phase field simulations of microstructure evolution in IN718 using a surrogate Ni–Fe–Nb alloy during laser powder bed fusion, Metals 9 (1) (2019).

[40] Wenjia Xiao, Simeng Li, Cunshan Wang, Yan Shi, Jyotirmoy Mazumder, Hui Xing, Lijun Song, Multi-scale simulation of dendrite growth for direct energy deposition of Nickel-based superalloys, Mater. Des. 164 (2019) 107553.

[41] Geoffrey B. Mcfadden, Sam R. Coriell, Robert F. Sekerka, Effect of surface free energy anisotropy on dendrite tip shape, Acta Mater. 48 (12) (2000) 3177–3181.

[42] Vigo Pontevedra, Zhixin Tu, Yajun Yin, Jianxin Zhou, Xiaoyuan Ji, Xu Shen, Sciencedirect sciencedirect sciencedirect a taylor approximation scheme for coupling thermodynamic data a taylor approximation scheme for coupling thermodynamic data of multicomponent alloy conference in phase-field model of multicomponent alloy in costing models for capacity optimization in industry 4 . 0 : Trade-off between used capacity and operational efficiency, Procedia Manuf. 37 (2019) 633–640.

[43] John W. Cahn, John E. Hilliard, Free energy of a nonuniform system. I. Interfacial free energy, 1958.

[44] Andrew Martin Mullis, J. Rosam, Peter K. Jimack, Solute trapping and the effects of anti-trapping currents on phase-field models of coupled thermo-solutal solidification, J. Cryst. Growth 312 (11) (2010) 1891–1897.

[45] Xueqin Huang, Joel Berry, Aurélien Perron, Raymundo Arróyave, A comparative study of kim-kim-suzuki (kks), partition coefficient relaxation (pcr), and finite interface dissipation (fid) phase field models for rapid solidification, Addit. Manuf. 74 (2023) 103704.

[46] Wenjia Xiao, Simeng Li, Cunshan Wang, Yan Shi, Jyotirmoy Mazumder, Hui Xing, Lijun Song, Multi-scale simulation of dendrite growth for direct energy deposition of Nickel-based superalloys, Mater. Des. 164 (2019) 107553.

[47] Brandon M. Lane, Sergey Mekhontsev, Steven E. Grantham, Mihaela Vlasea, Justin G. Whiting, Ho Yeung, Jason C. Fox, Clarence J. Zarobila, Jorge E. Neira, Michael L. McGlauflin, Leonard M. Hanssen, Shawn P. Moylan, M.A. Donmez, Joseph P. Rice, Design , developments , and results from the nist additive manufacturing metrology testbed (ammt), 2016.

[48] Jarred C. Heigel, Brandon M. Lane, Measurement of the melt pool length during single scan tracks in a commercial laser powder bed fusion process, J. Manuf. Sci. Eng. Trans. the Asme 140 (5) (2018) 1–8.

[49] Richard E. Ricker, Jarred C. Heigel, Brandon M. Lane, Ivan Zhirnov, Lyle E. Levine, Topographic Measurement Of Individual Laser Tracks In Alloy 625 Bare Plates, vol. 8, (4) 2019.

[50] Jarred HeigelBrandon LaneBrandon Lane, The effect of powder on cooling rate and melt pool length, 2017, pp. 1340–1348.

[51] Supriyo Ghosh, Li Ma, Nana Ofori-Opoku, On The Primary Spacing and Microsegregation Of Cellular Dendrites In Laser Deposited Ni-Nb Alloys, 1–25.

[52] Omid Emadinia, Fahad Zafar, Felipe Klein Fiorentin, Ana Reis, Effect of heat accumulation on the microstructural evolution in inconel 625 superalloy printed by ded process, Procedia Struct. Integr. 53 (2024) 278–284.

[53] Jeff P. Simmons, Chen Shen, Yi Z. Wang, Phase field modeling of simultaneous nucleation and growth by explicitly incorporating nucleation events, Scr. Mater. 43 (10) (2000) 935–942.